

TECHNICAL REPORT

Detector Geometries for Coherent X-Ray Diffractive Imaging at the SPB Instrument

August 2013

*K. Giewekemeyer, Scientific
Instrument SPB (WP84); M. Turcato,
Detector Development (WP75);
and A.P. Mancuso, Scientific
Instrument SPB (WP84)*

European X-Ray Free-Electron Laser Facility GmbH

Albert-Einstein-Ring 19

22761 Hamburg

Germany



Contents

1	Introduction	4
1.1	Acknowledgements	5
2	Science cases for the SPB instrument	6
3	Effects of incomplete data in coherent diffractive imaging	9
4	Numerical simulations—basic considerations	11
5	Considerations on the optimum AGIPD module layout	14
5.0.1	Dynamic range	15
5.0.2	Simulation strategy	15
5.1	Gap option	17
5.1.1	Tailored attenuators (non-feasible option)	18
5.2	Pile option	20
5.2.1	Layout	20
5.2.2	20 nm case	22
5.2.3	500 nm case	23
5.2.4	1500 nm case	26
5.3	Windmill option.....	27
5.3.1	Layout	27
5.3.2	20 nm case	29
5.3.3	500 nm case	30
5.3.4	1500 nm case	32
5.4	Summary and conclusion.....	33
6	Considerations on the optimum DSSC module layout	36
6.1	Overview of the relevant DSSC parameters	36
6.1.1	Dynamic range	36
6.1.2	Simulation strategy	37
6.1.3	Considerations on the geometry and hexagonal pixel shape	37
6.2	Windmill option.....	41
6.3	Baseline (pile) option	43
6.4	Summary and conclusion.....	49
7	Overall conclusions	51

8 Bibliography 54

1 Introduction

The Single Particle, Clusters and Biomolecules (SPB) instrument will be one of the six initial scientific instruments at the future European XFEL facility [8]. Its main applications will be nanocrystallography and coherent imaging of single particles, both techniques with challenging demands for detector technology.

The Active Gain Integrating Pixel Detector (AGIPD) [4], one of three dedicated detector projects for the European XFEL, will be the primary detector at the SPB beamline, which is planned to operate in a photon energy range from ca. 3 keV to ca. 15 keV. In addition, the Depleted P-Channel Field Effect Transistor (DEPFET) Sensor with Signal Compression (DSSC) detector is planned to be used predominantly at the lower photon energy range of the instrument. With an optimum working point of 3 keV, the DSSC detector complements the AGIPD detector, which works most efficiently at 12 keV and can be used readily down to ca. 5 keV.

The present document details some of the technical requirements for both detectors in the context of planned experiments at the SPB instrument. More specifically, we evaluate possible module layouts and experiment geometries in order to best serve the broad scientific scope of the SPB instrument. Importantly, the advantages of a variable hole size for the AGIPD and DSSC detectors at the SPB beamline are illustrated by numerical simulations.

We concentrate on the case of non-crystalline particles, i.e. we do not consider crystalline materials here. For the latter type of samples, the hole size is less restrictive. Nevertheless, there being a requirement for non-crystalline samples (see below), a second detection plane is possibly useful for crystalline samples as well, namely by aiding the phasing of the crystal diffraction patterns [1].

Note that the simulated geometries shown here do not represent optimal solutions in a mathematical sense. They have been obtained by careful comparison of simulated test cases for different reasonably chosen geometrical parameters. As a consequence, minute improvements to the quality of the final combined diffraction patterns may still be possible if two detection planes are used. These improvements, however, would only have a small overall effect and would not alter the general conclusions of this document.

1.1 Acknowledgements

We would like to thank the members of the AGIPD and the DSSC consortia for continuous feedback and for sharing technical details of the planned detector designs. We thank Andrew Aquila for his initial work on this matter, which initiated the considerations presented here, and we acknowledge fruitful discussions with Andreas Scherz on the DSSC detector implementation.

2 Science cases for the SPB instrument

The main scope of the SPB instrument will be to investigate single particle samples, which are predominantly injected into the X-ray free-electron laser (XFEL) beam by liquid-jet or aerosol techniques. In contrast to fixed-target samples, a stream of sample particles allows the application of the so-called “diffract-and-destroy” principle, where one particle at a time is hit by a single pulse of the XFEL beam [1]. This pulse (lasting on the order of 50 fs and less) is short enough that the scattering signal from a particle is collected on the detector before the particle is, inevitably, destroyed by the Coulomb explosion that is initiated by the interaction of the strong X-ray field with the particle.

Though it is envisioned that fixed-target samples will also be investigated, the majority of samples will be of the injected, single-particle type. These, furthermore, fall into three major categories: nanocrystals (NX), reproducible single particles (SPR), and non-reproducible single particles (SPnR). In contrast to the first group, the latter two are not crystalline and thus generally have detector requirements different from the crystalline samples that produce well-isolated Bragg spots on the detector.

The differences in typical expected diffraction patterns from the three groups of samples are illustrated in Figure 2.1, Figure 2.2, and Figure 2.3.

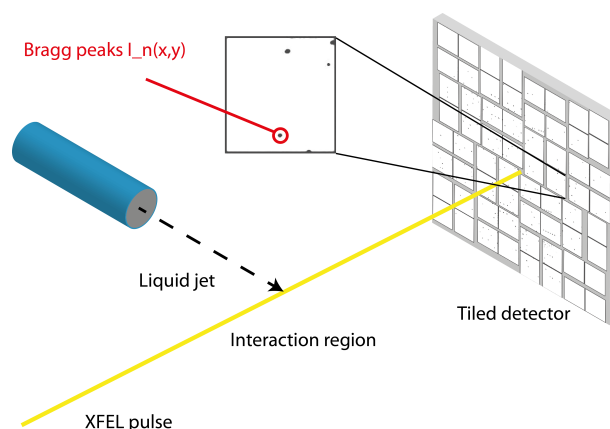


Figure 2.1: Illustration of a protein-crystallography experiment with an example data frame. The crystalline structure of the sample induces a diffraction pattern with isolated Bragg peaks of high intensity, well above the background. Provision of the diffraction pattern used for this image is a courtesy of Karol Nass and Thomas White, CFEL.

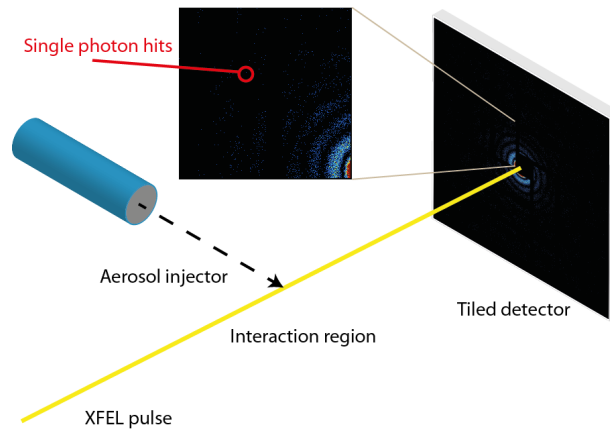


Figure 2.2: Illustration of a single particle experiment with a typical reproducible bio-particle, e.g. a single, large molecule ($10 \text{ nm} \lesssim \varnothing \lesssim 50 \text{ nm}$). The diffraction pattern (sketched here on logarithmic scale) is continuous but so weak that the vast majority of pixels contains none or only a single photon.

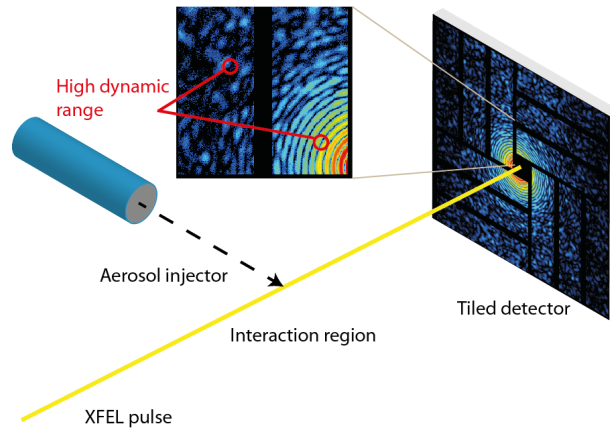


Figure 2.3: Illustration of a single particle experiment with a typical non-reproducible, larger bio-particle ($100 \text{ nm} \lesssim \varnothing \lesssim 3 \text{ }\mu\text{m}$). The diffraction pattern (shown on a logarithmic scale) is continuous, and its intensity spans many orders of magnitude.

In addition, the different requirements and experimental parameters for the three different cases are given in Table 2.1.

Table 2.1: Sample parameters for typical science cases for applications in biology. Note that applications in material science are also expected. Here, however, one can usually expect much stronger scattering signals due to the heavier elements typical for material science samples. This increases the demand for high dynamic range.

	Reproducible single particles (SPR)	Nano-crystallography (NX)	Non-reproducible single particles (SPnR)
Typical samples from biological sciences	Macromolecules, viruses	Protein nanocrystals	Viruses, organelles, bacteria, small eukaryotes
Photon energy	ca. 3–6 keV	ca. 8–16 keV	ca. 3–6 keV
Sample size	ca. 10 nm – 500 nm	ca. 100 nm – 2 μ m	ca. 100 nm – 3 μ m
Images per dataset	On the order of 100 000 – 1 000 000 and more	On the order of 10 000	1
Dimensionality of reconstruction	3	3	2
Single photon sensitivity	Critical	No	Beneficial, but not critical
Dominant signal levels in one measured pattern/pixel	0–10 photons	ca. 10^2 – 10^4 photons and more	0– 10^8 photons and more
Sampling / number of pixels	Detector linear extent (pixels) $\cong 4 \times$ number of resolution elements required (allows for adequate sampling of speckles); higher sampling favored	Detector linear extent (pixels) $\cong 10 \times$ number of resolution elements required (i.e. ~ 10 pixels between Bragg peaks)	Detector linear extent (pixels) $\cong 4 \times$ number of resolution elements required (allows for adequate sampling of speckles)
Sensitivity to missing data regions	Sensitive, low-q information critical, many images beneficial	Not sensitive, low-q information not needed	Very sensitive, can prohibit unique reconstruction

3 Effects of incomplete data in coherent diffractive imaging

At the heart of (plane wave) coherent X-ray diffractive imaging (CDI) lies an adequately sampled measurement of the continuous diffraction pattern generated by an isolated particle, e.g. a virus, biological cell, or inorganic nanoparticle [12, 9, 15]. Quite generally, this diffraction pattern is characterized by a strong central peak and a rapid decay in the radial, outward direction, following roughly a power law with an exponent between approximately -3 and -4 [6]. There is a Fourier transform relation of the diffraction pattern with the exit wave of the sample, or—in a diffraction rather than an optical picture—with the electron density distribution of the sample. This implies that the diffraction data close to the centre encodes the low spatial frequencies, i.e. the overall sample size and shape, whereas the high angle data encodes high-resolution features of the sample.

The high dynamic range of the diffraction pattern—for strongly scattering samples, often six orders of magnitude or potentially much more—usually necessitates the direct beam being blocked by a beam stop, which inevitably also covers some low-angle scattering contributions from the sample. For the application at free-electron lasers (FELs), the beam stop has to be replaced by a central hole in the detector to let the direct beam pass through, as the direct FEL beam can be stopped only if its cross-section is much larger compared to the focus. For the analysis, both a large beam stop upstream of the detector and a central hole lead to missing data regions close to the centre of the diffraction pattern. In addition, most current detector designs for FEL studies include a modular arrangement of photon-sensitive detection areas, with non-sensitive areas in between. In addition to the non-sensitive central regions, these so-called “dead areas” can also influence the feasibility of reconstructions considerably.

The effect of missing data regions, especially close to the centre of the diffraction pattern, has been studied previously [16, 5, 13]. In essence, a fully quantitative reconstruction of the diffraction pattern, i.e. a measurement of the sample’s electron density distribution, is possible only if the missing data region is smaller than the

central speckle.¹ Otherwise, the reconstructed image can at best be a non-unique, high-pass filtered representation of the object transmission function with no quantitative meaning. In addition, the iterative reconstruction methods used in CDI strongly depend on a good definition of the sample support, which can only be obtained if sufficient low-angle data has been collected.

As a consequence, the size of the missing data near the centre of the diffraction pattern has to be minimized without damaging the detector by moving its sensitive area too close to the intense, direct beam.

To this end, two strategies can be applied. The first is to use one detection plane and to make the central hole as small as possible in order to lose as little information as possible. The risk here, in particular for large samples in the micron range, is to miss this central information anyway and also to damage the detector with the very bright low- q scattering contribution. Alternatively, one can intentionally increase the central hole and use a second, downstream detector to cover the low- q data close to the centre. This method necessitates bringing two noisy two-dimensional (2D) signals into one numerical detection plane for fast analysis using the discrete Fourier transform. This should be possible by interpolation of the low- q data onto the upstream detector plane, as the signal-to-noise ratio of the low- q data is likely to be high enough to do so. To our knowledge, so far, there is no example where the numerical combination of two detection planes has been shown in practice; nevertheless, this is not envisioned to be a fundamental problem.

The main advantage of two detection planes is a substantially increased dynamic range due to the smaller solid angle that is collected by the same pixel area in the downstream detection plane compared to the upstream detection plane. Thus, a downstream detector that is placed twice as far as the upstream detector receives one fourth of the flux per unit area. The dynamic range can be further increased by placing an attenuator in between both detectors. Furthermore, the same inactive pixel region appears smaller in q -space on the downstream detector, for the same reasons as just explained.

We will make an effort here to consider the one-plane case where it is feasible, as it is simpler, and make a transition to the two-plane case where the science case and detector constraints make it necessary.

¹A "speckle" here refers to a feature in Fourier space of characteristic diameter that is inversely proportional to the diameter of the imaged object if this is confined to a finite area. More precisely, the diameter of a speckle in Fourier space is $\Delta q = 2\pi/D$ if D is the diameter of the object in real space [17]. Note that sometimes the terms "speckle" and "fringe" are used in close connection. Fringes appear instead of speckles when the object has certain symmetries at the considered length scale, i.e. is spherical or essentially one-dimensional only. In these cases, the fringe period plays the same role as the diameter of a speckle in other cases.

4 Numerical simulations—basic considerations

The numerical simulations that were carried out for preparing this document are based on some (simplifying) assumptions, which are briefly outlined here.

For illumination, an ideal, fully coherent and monochromatic Gaussian focus is assumed with an intensity FWHM of either 3 μm (largest focus), 1 μm (large focus), or 100 nm (small focus).¹ All diffraction patterns were simulated with a total number of 10^{12} photons, a number that can be expected for a single pulse produced by the European XFEL.

The sample is considered to be thin enough for the projection approximation to be valid, i.e. the diffraction pattern on the detector is calculated by forming the (norm-preserving) 2D Fourier transform of the sample exit wave, which in turn is formed as the product of the complex illumination wave field in the focus and the complex sample transmission function. For the projection approximation to be true, generally the condition $\Delta_z < d_{\text{res}}^2/\lambda$ has to be obeyed, with Δ_z denoting the thickness of the sample, d_{res} the obtained resolution, and λ the photon wavelength [2, 3]. As an example, for a photon energy of 5 keV ($\lambda = 2.48 \text{ \AA}$) and a resolution of 5 nm, the maximum thickness, within which the projection approximation is valid, is on the order of 100 nm. Note that, in the initial simulated diffraction patterns, the approximate resolution limit of the projection approximation is marked by a green circle in the diffraction pattern. As the overall number of photons is not expected to change considerably, even if the projection approximation is replaced by a more accurate model, valid conclusions can be drawn from the simulations within the present context.

Noise is considered only in terms of the photon noise, i.e. Poissonian shot noise. No additional sources of noise, such as detector readout noise or physical noise, e.g. Compton background, are considered.

The sample itself is modelled as a homogeneous sphere of water containing a sample sphere with a diameter of 90% of that of the water sphere. The sample sphere is assumed to contain a random protein distribution of mean refractive index $\delta = 1.207 \times 10^{-5}$ and $\beta = 1.075 \times 10^{-7}$, and a relative standard deviation of 60%.

¹For the SPB instrument, two main different focal spot sizes are planned, one with around 100 nm FWHM and one with around 1 μm FWHM focal spot size. The actual size may be modified, e.g. by slits upstream of the focusing optics.

An example of the sample exit wave (the product of the complex illumination function and the sample transmission function) is shown in Figure 4.1. It is evident from the figure that a biological sample with a diameter of 500 nm is, to a very good approximation, a pure phase sample at a photon energy of 5 keV.

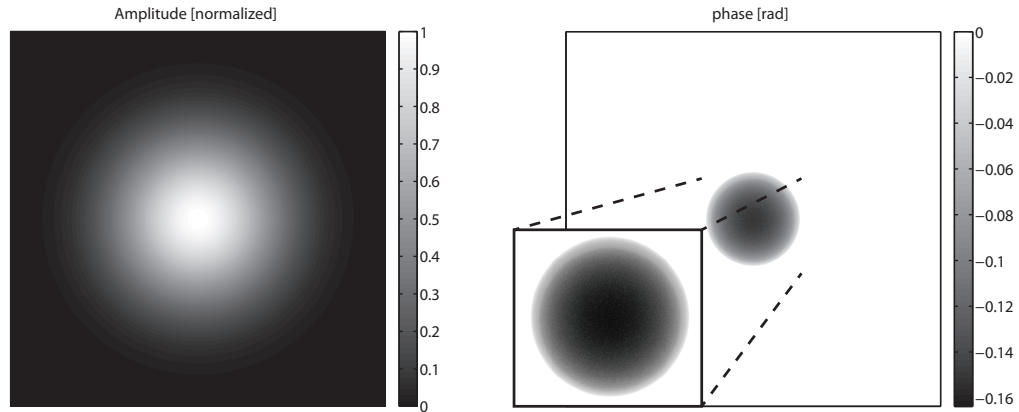


Figure 4.1: Amplitude (left) and phase (right) of the sample exit wave corresponding to an aqueous sphere with a diameter of 500 nm containing a protein sphere with a diameter that is 10% smaller. The field of view in both images is $2 \times 2 \mu\text{m}^2$. The inset in the right image gives a magnified view of the sample phase that indicates the random distribution of δ and β values inside the protein sphere.

All simulations for the AGIPD case have been carried out for a photon energy of 5 keV, which is an interesting wavelength both for very small biological particles and larger biological objects, as it provides relatively strong contrast with negligible absorption for most biological objects considered here. Thus, diffraction patterns have Friedel symmetry that may be employed for analysis, especially in the case of large, non-reproducible particles where only one 2D diffraction pattern is the basis for the iterative reconstruction process. For the DSSC case, an energy of 3 keV was assumed, the lowest possible energy at the SPB instrument and one of the optimum energies for the DSSC detector.

We have concentrated on three different sample cases, namely very small ones (20 nm diameter) such as large biomolecules, medium-sized ones (500 nm) such as viruses and organelles, and large-sized ones ($1.5 \mu\text{m}$) such as small cells. The third case is usually the most challenging, as the diffracted signal is strongest, the diffraction pattern spans many orders of magnitude, and the speckle size is the smallest.

The simulated cases are summarized in Table 4.1.

Table 4.1: Parameters for the different study cases considered in this document. Note that the number of detection planes refers to the optimum solution in each case.

Sample \varnothing / μm	Typical sample	Beam size (FWHM) / μm	Detection planes
0.02	Macromolecules	0.1	1
0.5	Viruses, organelles	1	2
1.5	Small cells	3	2

If two detection planes were considered in the simulation, the diffraction data was simulated in the upstream detection plane. The downstream contribution was obtained by interpolating the valid pixel regions (masks) on the downstream detector to the upstream detector grid. As a consequence, the actual diffraction data did not have to be interpolated and was simulated just in the upstream plane and then multiplied with the combined detector masks of both detection planes. For modelling the noise, it is important to include a possible attenuation factor for the downstream detector as well as the attenuating effect of the enlarged propagation distance.²

For all simulations, the relation between the missing central area, which is due to the central hole (gap), to the sample size has been evaluated. More specifically, the ratio

$$\chi = \frac{2\pi}{L} \frac{1}{q_{\text{lim}}} \quad (4.1)$$

has been calculated which corresponds to the ratio of the smallest spatial frequency in the diffraction pattern (essentially the size of a speckle) and the smallest spatial frequency that can be measured with the given hole (gap) size. In addition, the ratio was also calculated for the largest spatial frequency that can pass the central hole in a given situation and is thus available for a further measurement. Translated into real space, the ratio χ corresponds to the maximum linear extension that can be measured given a certain size of the hole divided by the linear extension of the sample. For a quantitative reconstruction to be feasible,

$$\chi > 1 \quad (4.2)$$

has to be fulfilled.

²For simplicity, these effects are included only as multiplicative factors, so that the noise in the downstream detection area is not modelled in the best possible physical way. The resulting error, however, should be relatively small. As an example, for a propagation distance factor of two between both detection planes, an ideal simulation forms the signal of a single pixel on the upstream detector by summing over four individual noisy pixels on the downstream detector. Here, we model the noisy signal corresponding to one pixel in the upstream plane directly.

5 Considerations on the optimum AGIPD module layout

The basic layout of a single AGIPD module is illustrated in Figure 5.1 [11]¹. One module consists of 16 application-specific integrated circuits (ASICs), each comprising 64 (horizontal) times 64 (vertical) pixels. The ASICs are arranged in two rows on top of each other, each comprising 8 integrated circuits. The monolithic Silicon sensor is placed on top of the ASIC layer. The pixel size is $200 \times 200 \mu\text{m}^2$, except for the pixels in columns at the edge of two neighbouring ASICs. These pixels are $400 \mu\text{m}$ wide and $200 \mu\text{m}$ high. In total, this leads to $512 + 14$ (horizontal) times 128 (vertical) quadratic, logical pixel units. For the simulation, these *logical* pixels are used even though some of them are physically grouped together in pairs into a single pixel. The active area of each module is enclosed by a guard ring with a width of 6 pixels and a wire-bonding ring with a width of 8.5 pixels on the horizontal edges and 0.5 pixels on the vertical edges. For the simulation these numbers are rounded up to integers.

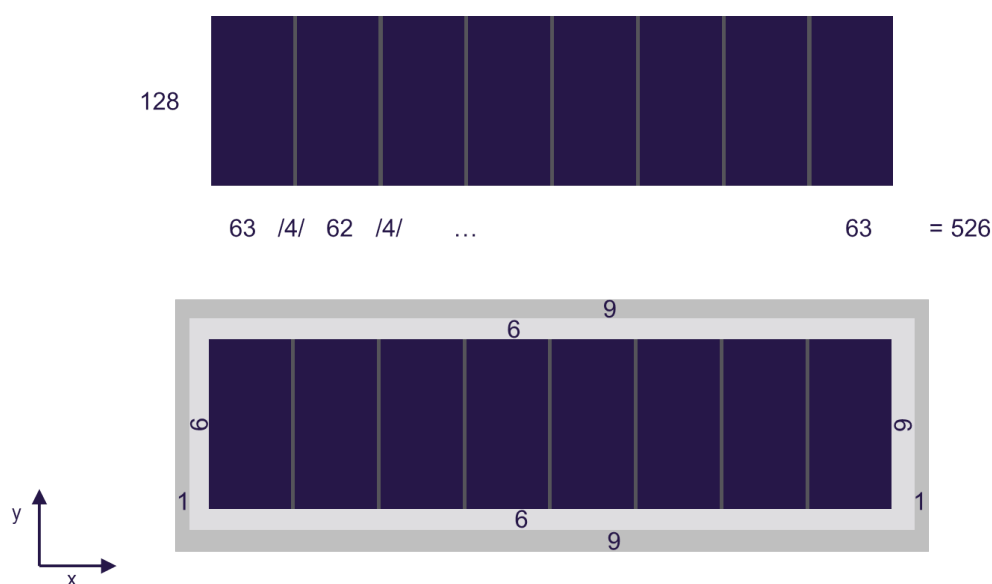


Figure 5.1: Schematic of the layout of a single AGIPD module. All numbers refer to pixels of unit size $200 \times 200 \mu\text{m}^2$. Note that some of the pixels, namely those in the gray vertical columns, are actually twice as large in horizontal direction, so that four units correspond to two measuring pixels.

¹The layout is subject to minor revisions by the AGIPD consortium.

There are three basic layouts for the AGIPD detector that are considered here: the so-called “gap” option, the “pile” option, and the “windmill” option.

In all three cases, we assume that 16 modules (1 megapixel) can be organized into one detection plane with a second, downstream detector option consisting of two (or four) AGIPD modules.

5.0.1 Dynamic range

The dynamic range of the AGIPD detector is energy-dependent. Here, a pixel was considered to be saturated above a count level of 24 480 photons at a photon energy of 5 keV. This value is obtained if a maximum well depth of 3.4×10^7 [14] is assumed, given an energy of 3.65 eV per created electron-hole pair in the active area of the detector [11].

5.0.2 Simulation strategy

As mentioned above, the goal is to determine the simplest layout in a series of experimental cases for the measurement of a complete, and thus likely reconstructible, dataset. Therefore, we start with the case of one detection plane and try to determine the lowest possible sampling ratio, i.e. the highest workable resolution. In the small-angle approximation, the linear sampling ratio σ , the real-space pixel width Δx , and the number of pixels in the detector along the considered coordinate direction are connected with the linear extension L of the sample via

$$\sigma = \frac{N\Delta x}{L}. \quad (5.1)$$

The real space pixel size Δx , i.e. the best geometrically achievable half-period resolution of the experiment under given conditions, is (in the small angle approximation) given by

$$\Delta x = \frac{\lambda z}{N\Delta X} \quad (5.2)$$

where ΔX denotes the detector pixel width, λ the photon wavelength, and z the distance from the sample to the detector. For a given sample size, wavelength, and detector pixel size, changing the sample–detector distance is the only way to influence the sampling ratio. A sampling ratio of 4 is considered as the smallest

practically feasible value.²

For these simulations, a central hole as small as possible with respect to the central beam and sample scattering is chosen first. Afterwards, the sampling ratio (i.e. the sample-to-detector distance) is increased enough that a considerable amount of the central speckle becomes measurable, while still maintaining a useful resolution.

If this does not lead to a workable solution, i.e. if the central speckle cannot be adequately measured, two detection planes at a reasonable sampling rate are then considered. This greatly increases the number of possible detector configurations. The first plane here is chosen to be as close to the sample as possible in terms of sampling.

For the case of two detection planes, the following general strategy for finding a good detector configuration was applied:

- 1 Translate the beam centre on the detector by half the width of the non-sensitive pixel gaps between modules in horizontal and vertical directions. This makes the use of Friedel symmetry³ possible in later analysis.
- 2 Increase the gap width to at least twice this translation distance, so that the detector modules are less likely to be saturated. To keep the symmetry (i.e. a square hole), choose the maximum hole width for both coordinate directions.
- 3 If necessary, increase the gap width further (so that neither tails of the direct beam nor sample scattering lead to detector saturation in the upstream plane), use a reasonable attenuation before the second plane, or both.

Note that presently there is no detailed consideration of an upper limit to the tolerable dose into a non-active detector region. In an update of the current simulations, this could be included.

²For single-molecule samples, e.g. a sampling ratio of 4 is not practically feasible as it requires the detector to be extremely close to the sample. Even with a very small central hole, only a very small part of the central speckle falls onto the active regions of the detector, if at all, thus requiring a higher sampling ratio.

³The term denotes the centrosymmetry of a diffraction pattern from a non-absorbing object. Within the projection approximation used for the simulations presented here, a non-absorbing, weakly scattering object can be described by a purely imaginary object transmission function that is proportional to the object's electron density, projected into the propagation direction. Such an object transmission function has a centrosymmetric Fourier transform.

5.1 Gap option

The basic design of the gap option is shown in Figure 5.2.

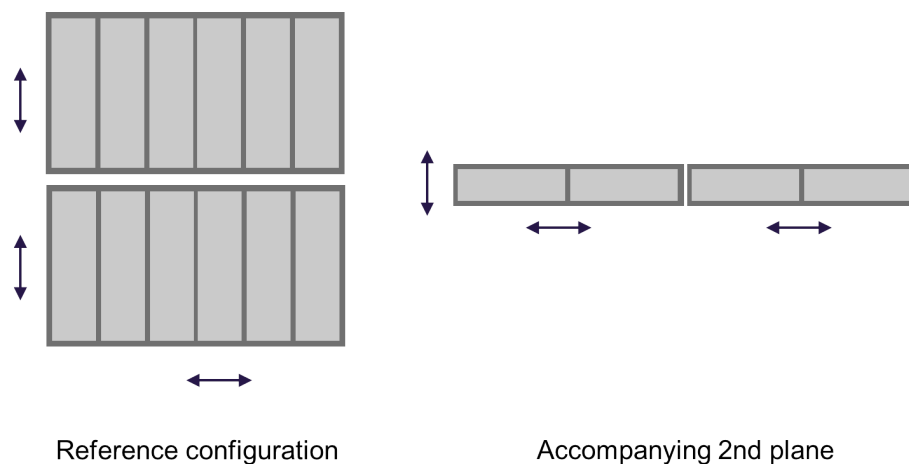


Figure 5.2: *Left:* Layout of the gap design, with two independently movable detector sections, adjustable in the horizontal and vertical direction. *Right:* Due to the large horizontal gap in the centre, a second downstream detector has to accompany the larger upstream detector. The modules are adjustable in vertical and horizontal direction. These motions may be synchronized.

In an effort to obtain a complete diffraction pattern, the upstream detector is equipped with two independent units with a horizontal gap in between. A downstream detector collects information in the regions that were not covered by the first detector.

This solution, however, exhibits a fundamental problem that is illustrated in Figure 5.3. Here, a 500 nm particle was simulated in a 1 μm beam. In order not to damage the downstream detector, the diffracted beam has to be attenuated prior to this plane. This is likely achieved by using a very homogeneous material, such as a single-crystal silicon wafer. For this simulation, an attenuation factor of 0.1 was assumed. As visible in the combined diffraction pattern, the diffraction signal is collected with a good signal-to-noise ratio (SNR) near the centre. The high- q area that is covered by the downstream detector, however, is not measured with an adequate SNR any more, as the attenuation becomes too strong for good signal in the high- q regions. This effectively demonstrates the limitations of the dynamic range of the detector.

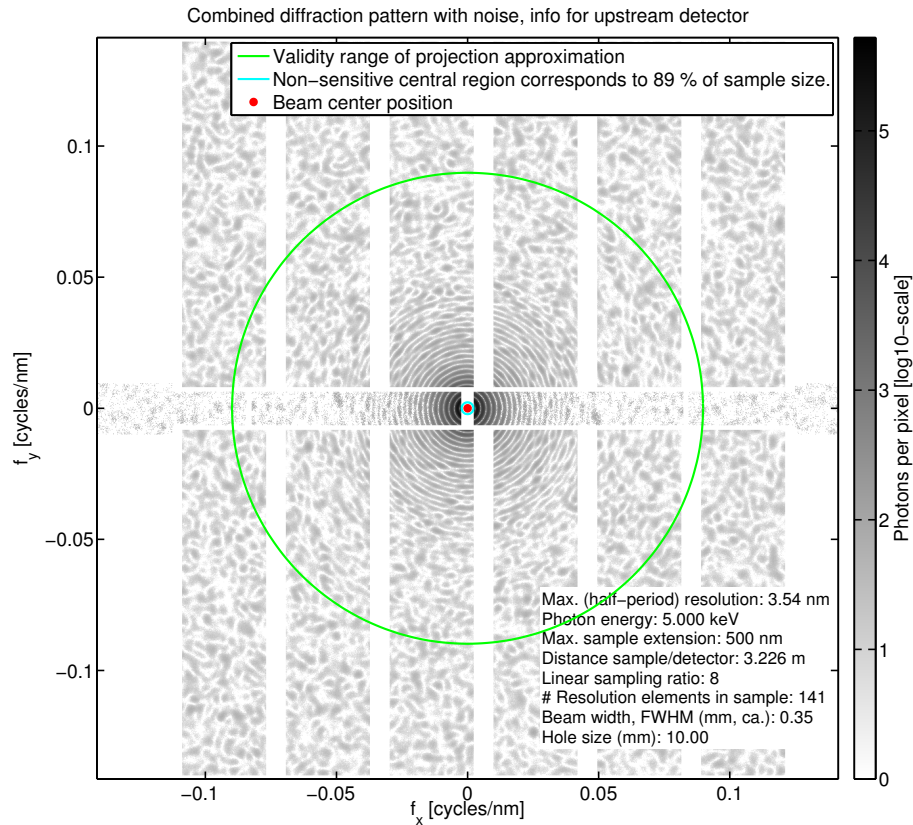


Figure 5.3: Simulated diffraction data from a 500 nm particle as seen by the upstream and downstream detector, combined in a single diffraction pattern by interpolation of the downstream data to the upstream data. Note that interpolation was done here before adding the noise. The green circle indicates the approximate validity range of the projection approximation, i.e. outside the circle, the physical diffraction pattern is likely to show some effects due to the non-zero curvature of the Ewald sphere. Usually, this leads to deviations from the central symmetry of the diffraction pattern.

5.1.1 Tailored attenuators (non-feasible option)

To solve this problem of insufficient SNR in the high- q regions of the downstream detector, one may propose specifically tailored attenuators, e.g. a circular attenuator with a central hole.

Note, however, that these attenuators would need to be designed separately for each sample size and each set of beam conditions (e.g. photon energy, spot size, etc.). It is rather difficult to take into account all possible types of expected diffraction patterns. These may be either rather isotropic (for nearly spherical particles) or very non-isotropic (e.g. for icosahedral or elongated virus particles or non-spherical organelles). In addition, sharp edges of the attenuators could produce parasitic

scattering effects in the diffraction pattern, lead to transition regions where the absorption is not constant over a single detector pixel, or both. Those pixels would be difficult to calibrate and would not be useful.

Furthermore, for the high-resolution diffraction data to be fully measured in the horizontal direction, the gap option implies a wide solid angle that needs to be clear of any equipment in order not to block the beam. If, however, the instrument for the Serial Femtosecond Crystallography (SFX) instrument is placed between the upstream and downstream detector, the required solid-angle may be partly covered by the SFX experiment chamber, its optics, or other instrumentation.

For these reasons, specifically tailored attenuators are regarded as an operationally implausible option. As a consequence, the gap solution is ruled out as a possible layout for the AGIPD detector at the SPB instrument.

Note, however, that under certain circumstances, the gap option might still be very useful if not required. More specifically, the strong unidirectional parasitic scattering caused by a water jet that is used to inject particles into the X-ray beam can, in some cases, be damaging to the detector and thus may need to be directed into a gap between modules. Therefore, four independently movable quadrants (which include the option of a gap) are very beneficial.

5.2 Pile option

The second option that was investigated here was the so-called “pile” option, which consists of four independently adjustable quadrants, each of which contains four modules “piled” up in the vertical direction (see Figure 5.4).

5.2.1 Layout

As a basic layout, a centrosymmetric arrangement of all four quadrants, each consisting of four modules, was assumed. The arrangement is chosen in such a way that the distance between neighbouring modules remains constant when the whole size is changed (see the caption of Figure 5.4). As a minor restriction in the simulations, the central hole was always assumed to have a squared shape. Note, however, that in some situations a different layout, such as with a vertical gap in between the left and right quadrants (see Figure 5.4), can be useful, so that ideally all four quadrants should be movable independently.

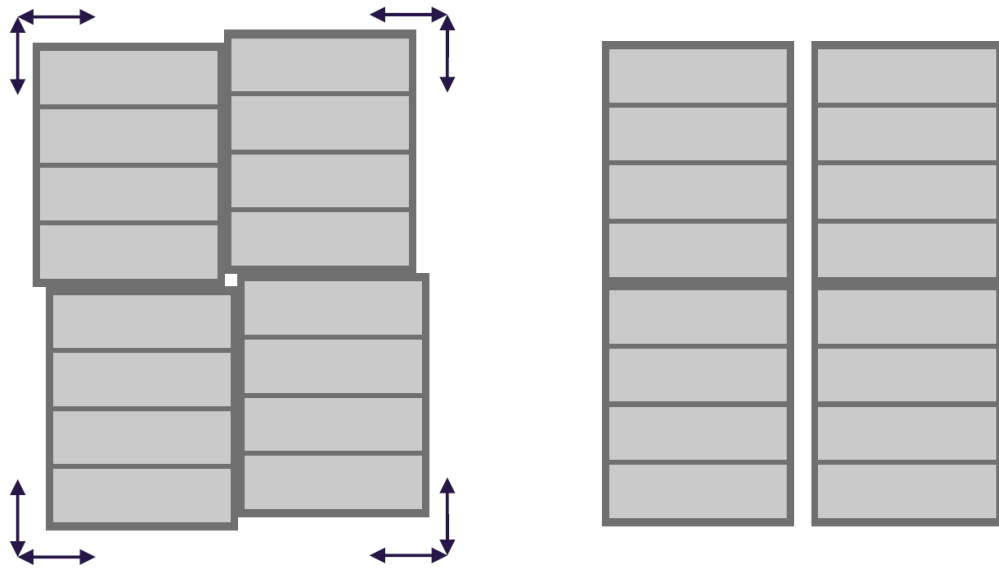


Figure 5.4: *Left:* Layout of the pile design, with four independently movable detector quadrants, each adjustable in the vertical and horizontal directions. Each quadrant consists of four modules aligned with their long side in the horizontal direction. Note that the layout shown here exhibits a point symmetry with respect to the centre. *Right:* Possible gap mode that can only be achieved if all quadrants can be moved independently.

If a second detector plane was used, a simple layout consisting of two AGIPD modules in gap mode, aligned with their long sides in horizontal direction, was

assumed. The same layout with four instead of two modules is shown in Figure 5.2 (right).

An example of a numerical mask created by the simulation code that was developed for the preparation of this document is shown in Figure 5.5. This shows the pile layout with a relatively large central hole.

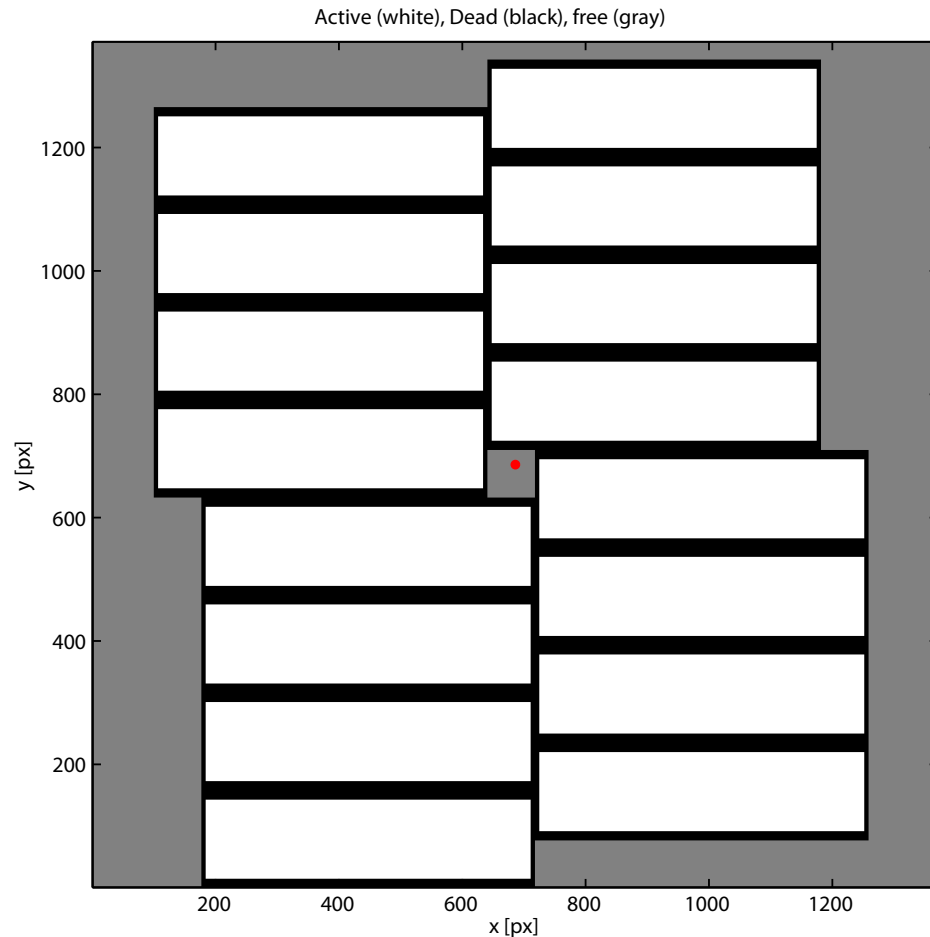


Figure 5.5: Example of the numerical mask corresponding to the pile layout. The red dot marks the position of the beam centre. Note that the configuration is such—with respect to the centre of symmetry of the mask, which is not the beam centre here—that each module is translated by the same distance with respect to the situation in which the hole is closed and all corners closest to the hole meet in the centre of symmetry of the mask. The translation directions are given by the edges of a square that is rotated by 45 degrees with respect to the coordinate axes. The surrounding gray area extends to the full extent of the numerical array, which is chosen in such a way that the beam centre is positioned at the centre of the numerical array.

5.2.2 20 nm case

As a first example for the pile layout, the case of a small particle ($\varnothing = 20$ nm) was considered. An example diffraction pattern is shown in Figure 5.6. The chosen sampling ratio of $\sigma = 25$ is a compromise between geometrically limited resolution and good access to the area of the central speckle. As for this type of sample, thousands of diffraction patterns are collected; the missing gaps can be filled up in the process of reconstruction of the three-dimensional (3D) Fourier space intensity using current algorithms, such as expansion–maximization–compression (EMC) [7]. As a consequence, Friedel symmetry does not need to be exploited, and the centre of symmetry of the detector and of the diffraction pattern can coincide.

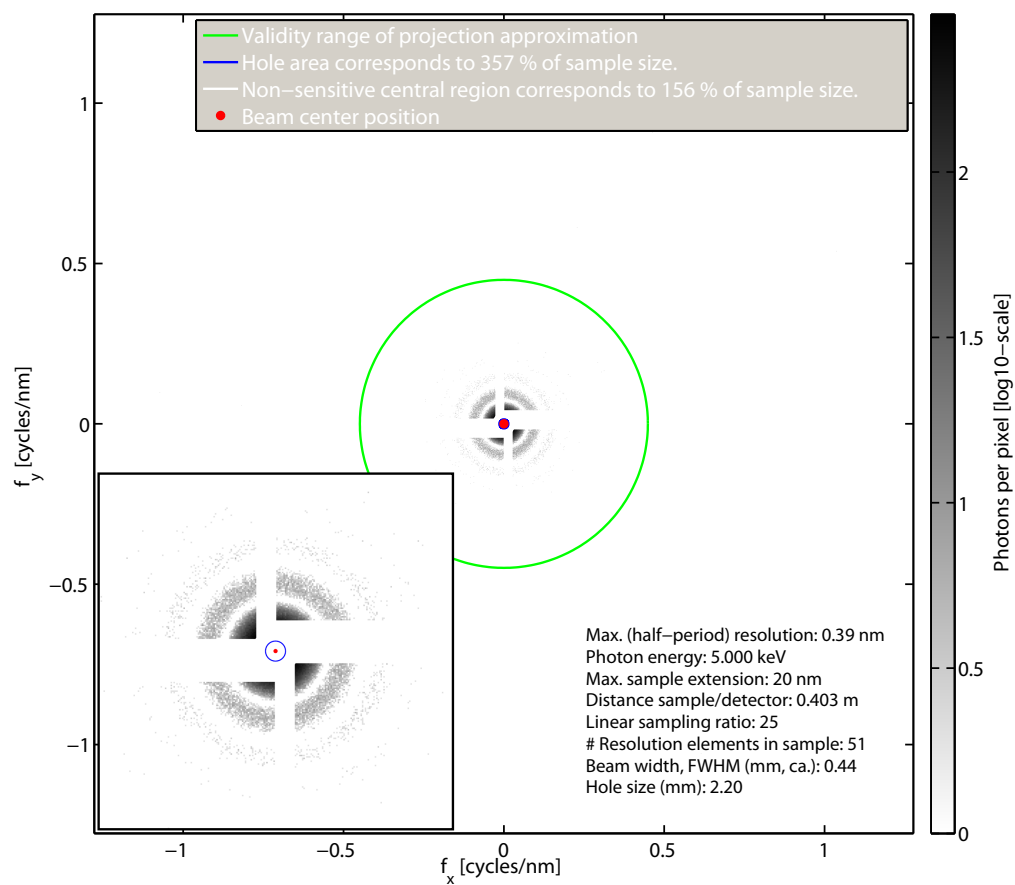


Figure 5.6: Simulated diffraction pattern for a 20 nm particle. Only one detector plane is used to record the diffracted photons. Note that large parts of the central speckle are recorded, even though there are large non-sensitive regions near the centre.

5.2.3 500 nm case

For a particle with a diameter of 500 nm, the measurable diffraction signal from a single shot extends over the whole detector area, even for a sampling ratio of $\sigma = 4$ (i.e. for the largest solid angle that can be covered by the detector in the accessible range of sampling ratios and detector distances). The central hole has been closed here as much as possible without reaching saturation. At this value of σ , the detector is placed so close to the sample that the central speckle and several diffraction orders fall into the hole area or non-sensitive central regions of the detector (see Figure 5.7). Therefore, in order to better cover the central part of the diffraction pattern, the detector has to be moved further away. This, however, means giving up resolution that is accessible in terms of the high-q scattering signal. The only solution that allows for both, the measurement of the central part *and* the high-resolution regions of the diffraction pattern, is thus to open up the central hole and to add a second detection plane at a second, larger detector distance.

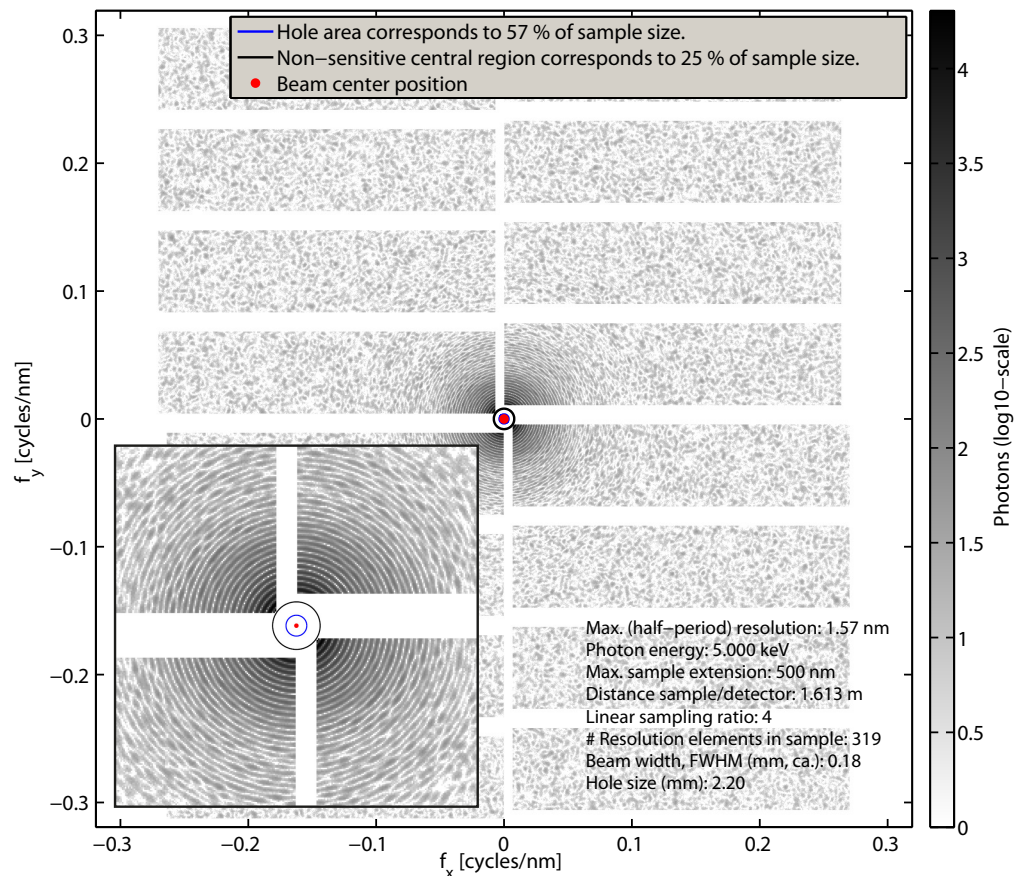


Figure 5.7: Simulated diffraction pattern for a 500 nm particle at a minimum sampling ratio of 4. Only one detector plane is used to record the diffracted photons. Note that the central speckle and further central fringes are not recorded at all at this sampling ratio.

A possible resulting combined diffraction pattern from two detectors is shown in Figure 5.8. To measure at least a part of the central speckle, the sampling ratio has been increased to a value of 8. This still allows for a half-period resolution of about 3 nm and thus 168 resolution elements along the sample diameter.

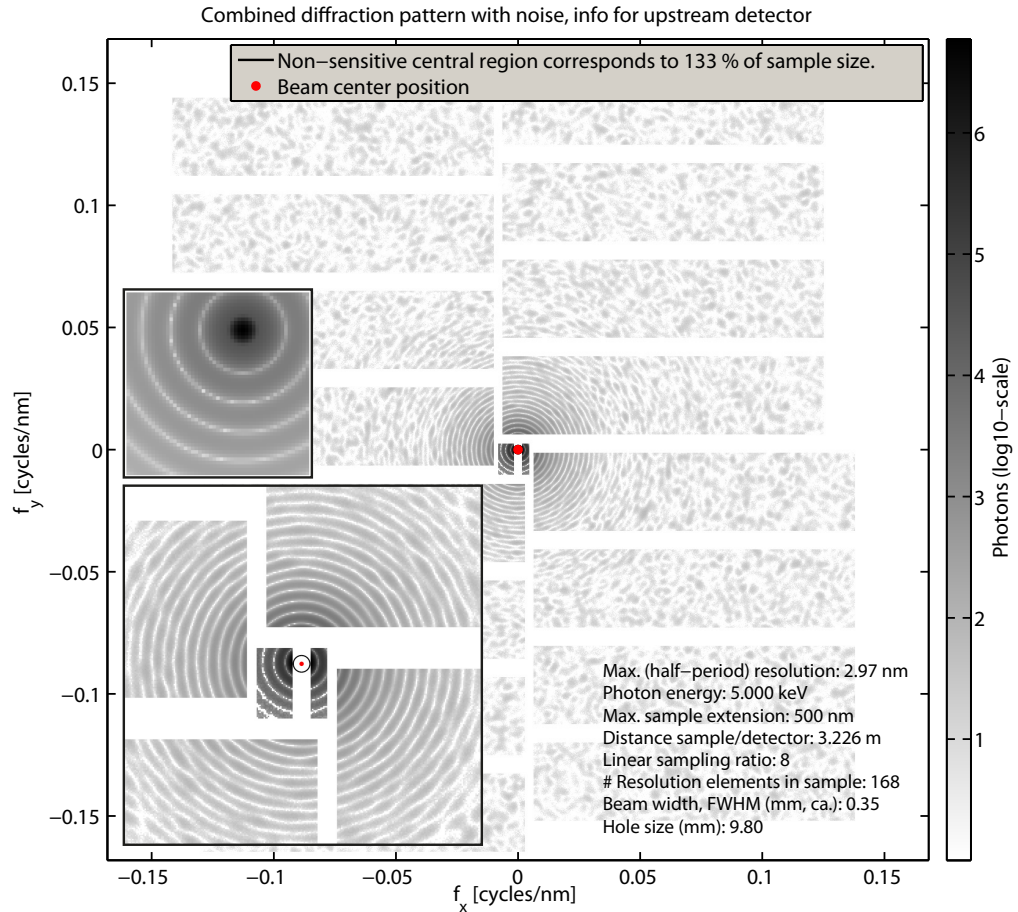


Figure 5.8: Simulated diffraction pattern for a 500 nm particle at a minimum sampling ratio of 8. Two detection planes are used to record the diffraction data. The large inset shows the central region of the combined diffraction pattern with noise. The small inset shows, for comparison, part of the diffraction pattern that corresponds to the area of the central hole in the upstream detector. It can be seen that the central speckle is partly measured. Note that the colour scale does not apply to the small inset.

As biological samples in the 500 nm–size range can usually be expected not to be reproducible, missing information due to non-sensitive detector areas cannot be filled up from several independently collected diffraction patterns. However, the central hole has been opened up here to about 1 cm, so that the detector can be translated in such a way that the Friedel symmetry of the diffraction pattern can be exploited to fill the non-sensitive regions of the detected pattern with information. Such a symmetry

completion is shown in Figure 5.9. According to our previous considerations about diffraction patterns with missing data, there should be no fundamental obstacles preventing a possible quantitative reconstruction of this diffraction pattern.

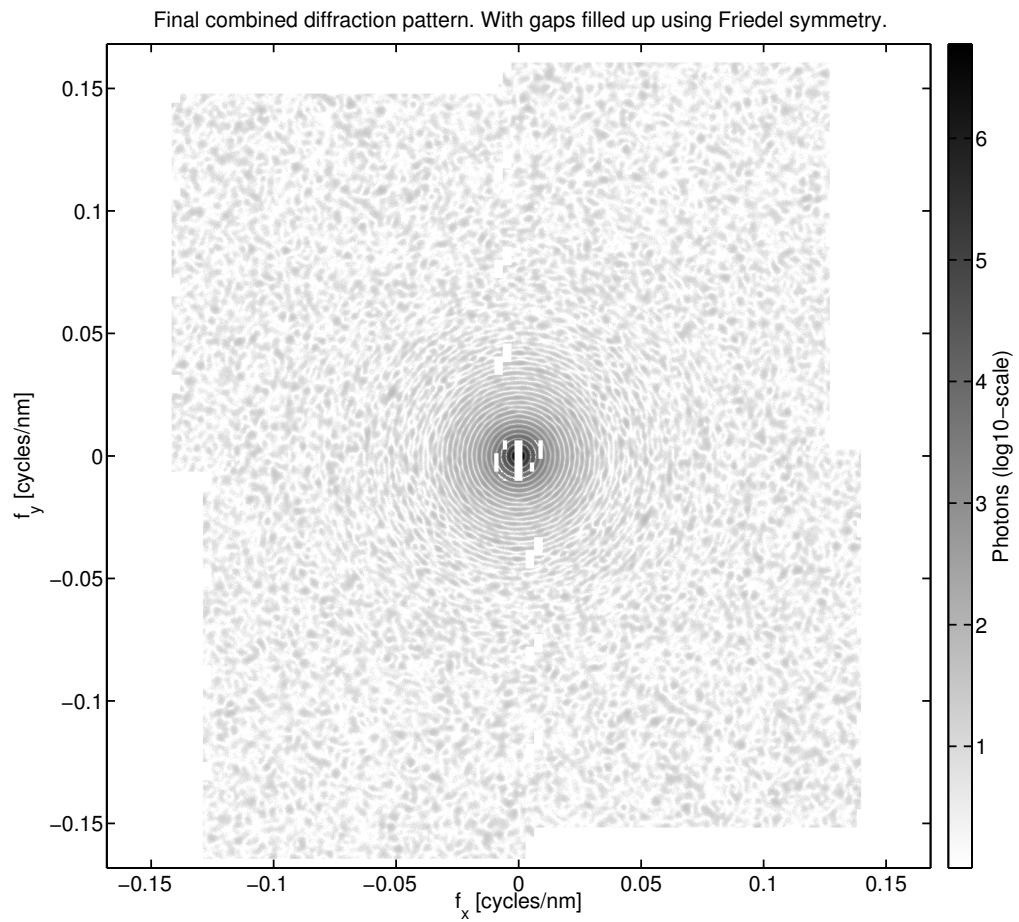


Figure 5.9: Simulated diffraction pattern obtained by filling up non-sensitive regions using Friedel symmetry. The original diffraction pattern from which this pattern was produced is shown in Figure 5.8.

5.2.4 1500 nm case

An even more challenging case is given by a sample size of 1.5 μm . Not only in terms of constraints due to sampling, but also in terms of the beam diameter, this sample size is at the limit of what can be measured at the SPB beamline with single-shot measurements. In Figure 5.10, a combined diffraction pattern for the current case is shown that is close to an ideal situation. However, as also visible from the images, the central speckle cannot be measured, so that a fully quantitative reconstruction becomes difficult. For such large particles, it is therefore recommended to decrease the energy to 3 keV and to use the DSSC detector for improved sampling.

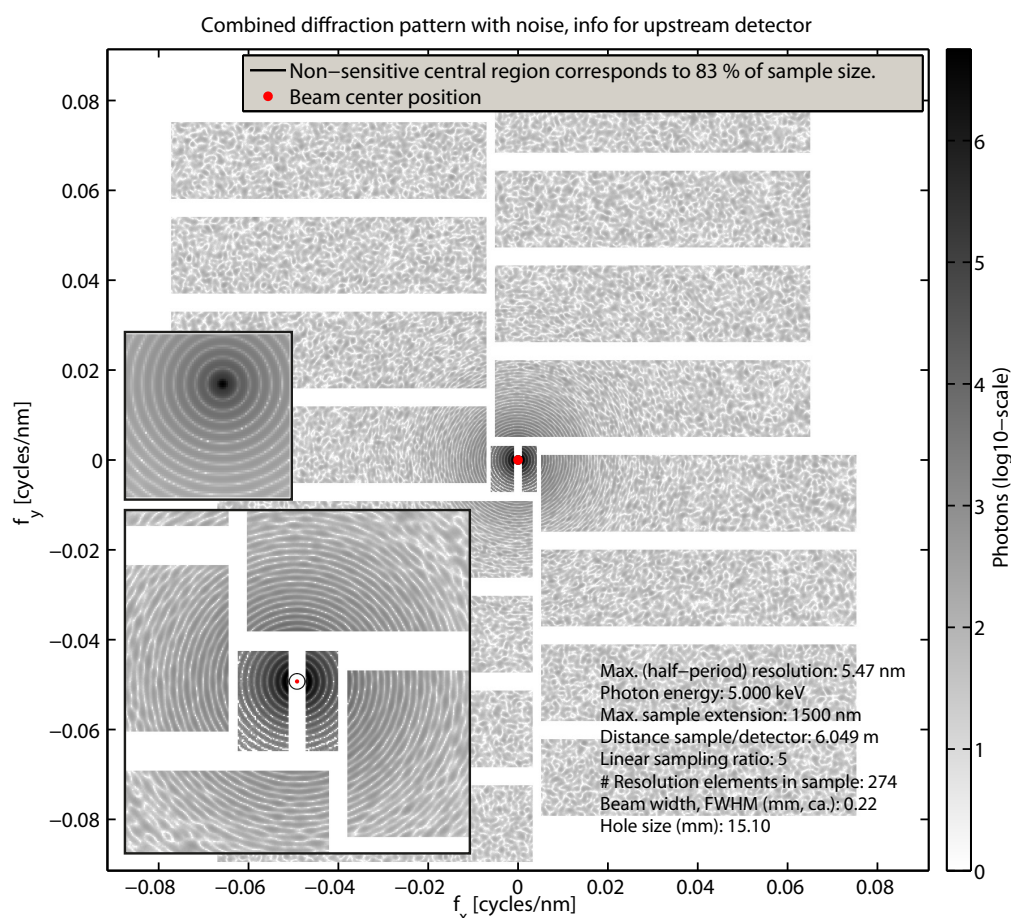


Figure 5.10: Simulated diffraction pattern for a 1500 nm particle at a minimum sampling ratio of 5. Two detection planes are used to record the diffraction data. The large inset shows the central region of the combined diffraction pattern with noise. The small inset shows, for comparison, part of the diffraction pattern that corresponds to the area of the central hole in the upstream detector. It can be seen that the central speckle is not measured, even partly. Note that the colour scale does not apply to the small inset.

5.3 Windmill option

The last considered layout is called the “windmill”, as the four individual quadrants, each containing four modules, are oriented in such a way that, when moving from one quadrant to the next one in clockwise direction, the next quadrant is always rotated by 90 degrees in clockwise direction with respect to the previous one.

5.3.1 Layout

Note that the windmill layout can be achieved in two distinct ways, with e.g. the upper right quadrant rotated so that the longer side of the individual modules is oriented vertically or horizontally. As the non-sensitive edge on each module is narrower on its shorter side than on its longer side, the option shown in Figure 5.11 (modules oriented vertically) has a slight advantage over its alternative: for a given size of the central hole, the distance from the edge of the hole to the nearest sensitive detector region becomes slightly smaller than in the alternative solution.

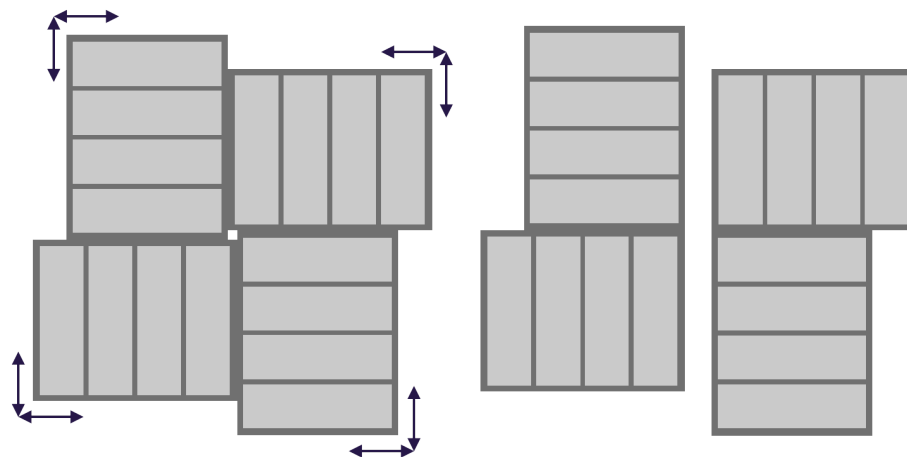


Figure 5.11: *Left:* Layout of the windmill design, with four independently movable detector quadrants, each adjustable in the vertical and horizontal directions. The modules are grouped together in such a way that the non-sensitive area in the centre becomes smallest: the narrower non-sensitive edge of each module is adjacent to the hole, rather than the wider edge that is parallel to the longer side of the modules. Just like the pile in its symmetric configuration, this layout exhibits a point symmetry with respect to the centre. *Right:* Possible gap mode that can only be achieved if all quadrants can be moved independently.

Just as for the pile case, if a second detector plane was used in the simulations, a simple layout consisting of two AGIPD modules in gap mode, aligned with their long sides in horizontal direction, was assumed. The same layout with four instead of two

modules is shown in Figure 5.2 (right).

The different simulation cases are outlined analogous to those in Section 5.2, “Pile option”. We do not describe the different cases in detail again.

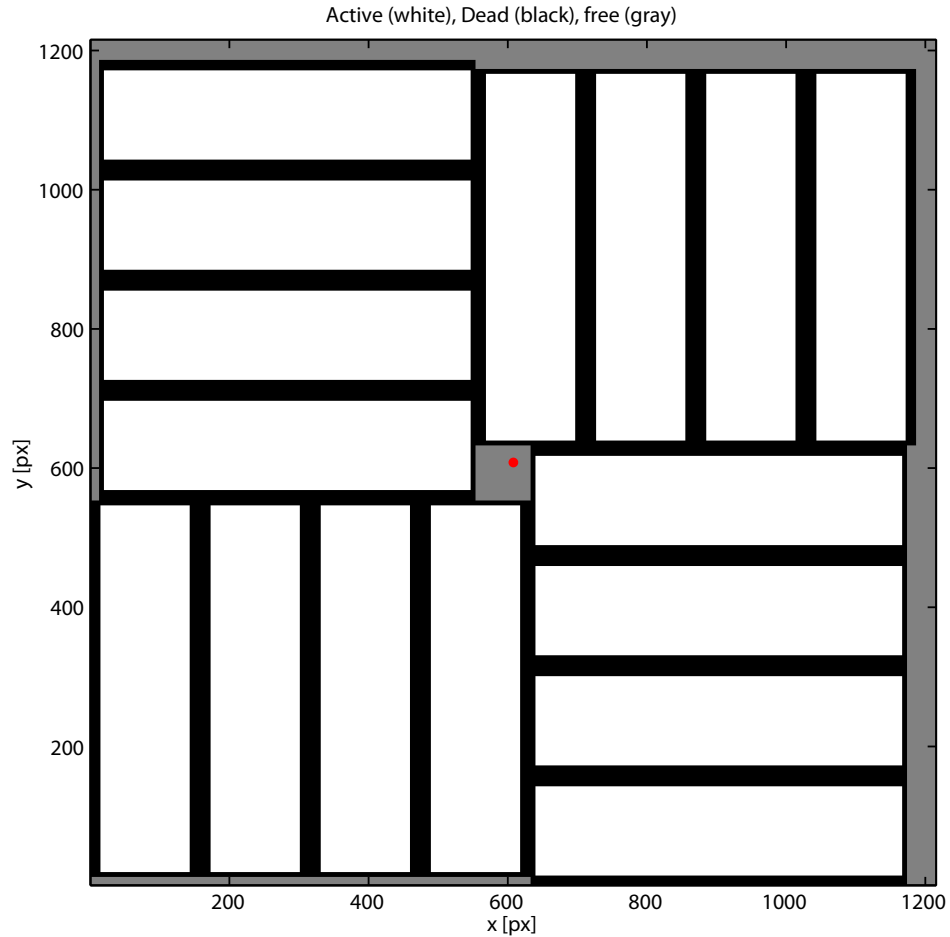


Figure 5.12: Example of the numerical mask corresponding to the windmill layout. The red dot marks the position of the beam centre. The centrosymmetric configuration of the four quadrants corresponds to the symmetric configuration of the pile layout (see above). Note that the overall layout is more quadratic than in the case of the pile configuration. This can be a considerable advantage in the analysis, especially in three dimensions, where cubic voxels are usually used.

5.3.2 20 nm case

As the first case, as in Section 5.2, “Pile option”, the diffraction from a small, 20 nm particle is considered. Here, one detection plane is sufficient, as missing regions in Fourier space can be filled up by combining many diffraction patterns into a 3D dataset in Fourier space. The simulated diffraction pattern for a 20 nm particle is shown in Figure 5.13.

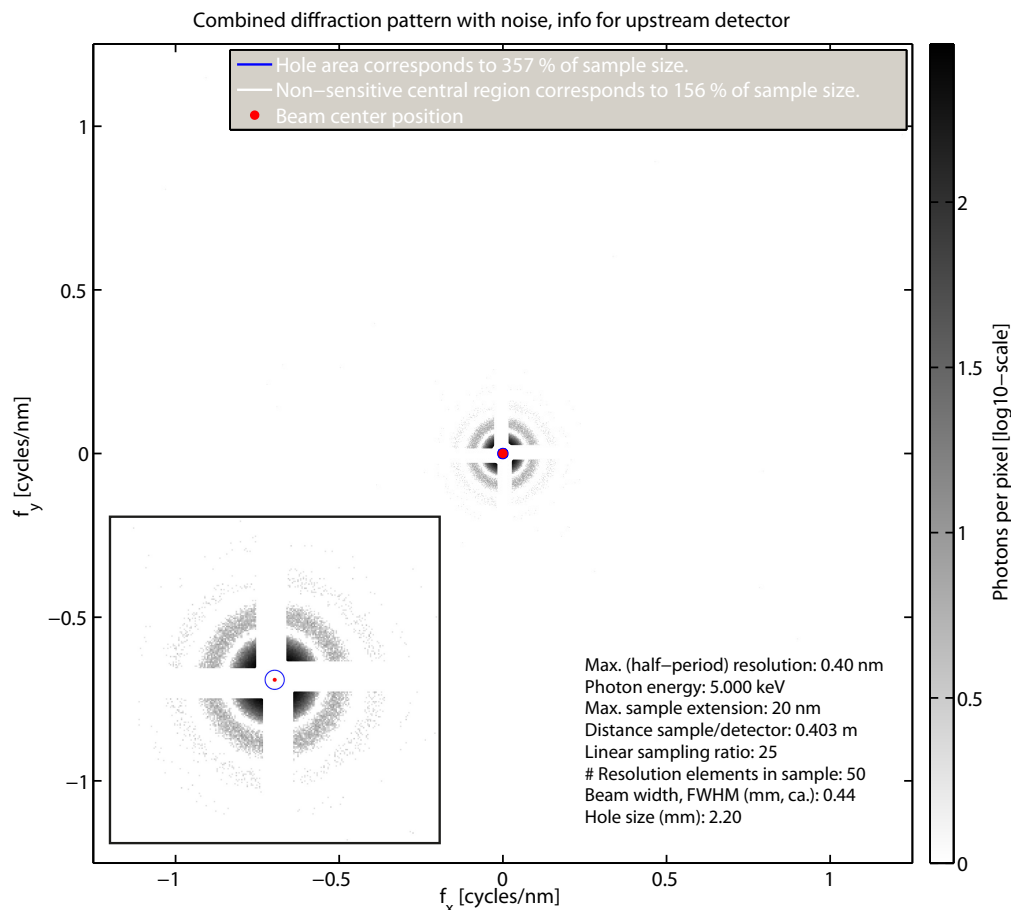


Figure 5.13: Simulated diffraction pattern for a 20 nm particle. Only one detector plane is used to record the diffracted photons. Note that larger parts of the central speckle are recorded than for the pile layout in the same experimental situation. In this configuration, the non-sensitive gaps are smaller than in the pile configuration. This disadvantage is, however, mitigated by the fact that many diffraction patterns can be used to fill up missing detector regions.

5.3.3 500 nm case

As in the case of the pile layout, the measurement of a full diffraction pattern from a particle of 500 nm diameter, at a reasonable resolution, is not possible with the given detector layout and parameters in a single detection plane. The reasons are the same, i.e. the dynamic range of the detector does not allow for a simultaneous measurement of diffraction data close to the centre and at the tails of the diffraction pattern. Therefore, we do not reiterate this case here and only show the results for two detection planes.

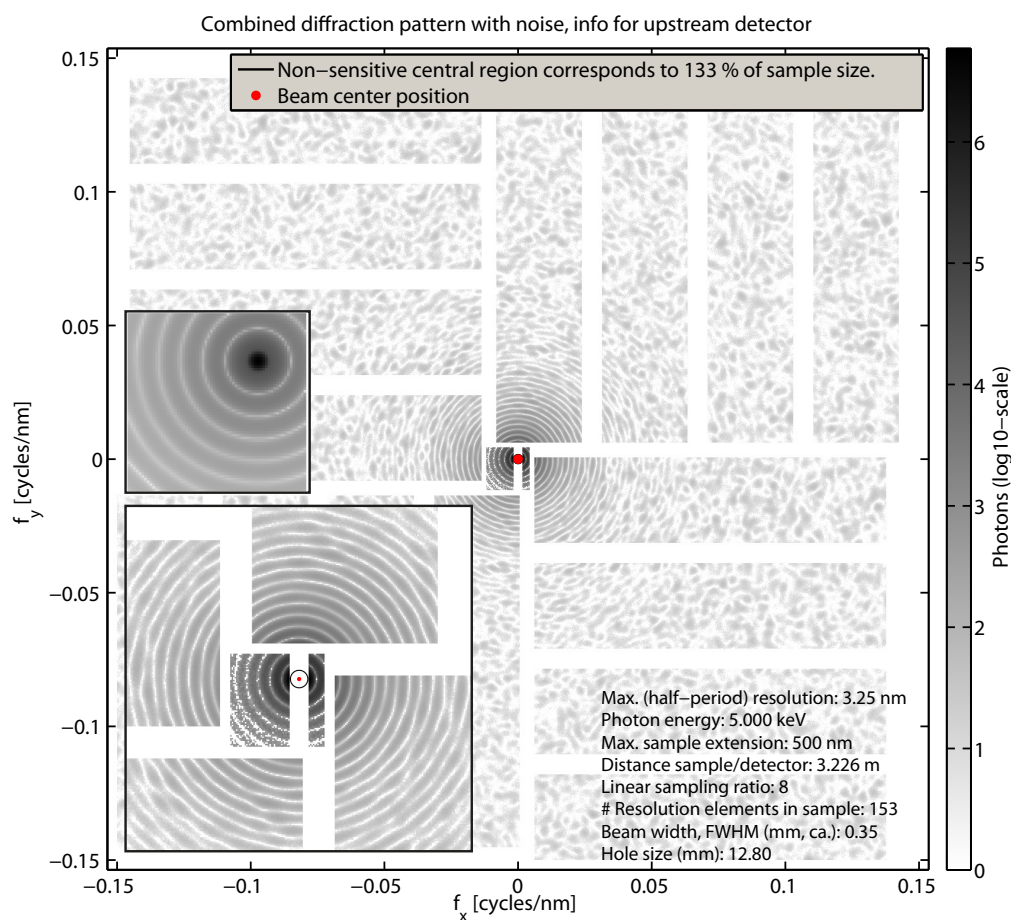


Figure 5.14: Simulated diffraction pattern for a 500 nm particle at a minimum sampling ratio of 8. Two detection planes are used to record the diffraction data. The large inset shows the central region of the combined diffraction pattern with noise. The small inset shows, for comparison, part of the diffraction pattern that corresponds to the area of the central hole in the upstream detector. It can be seen that the central speckle is partly measured. Note that the colour scale does not apply to the small inset.

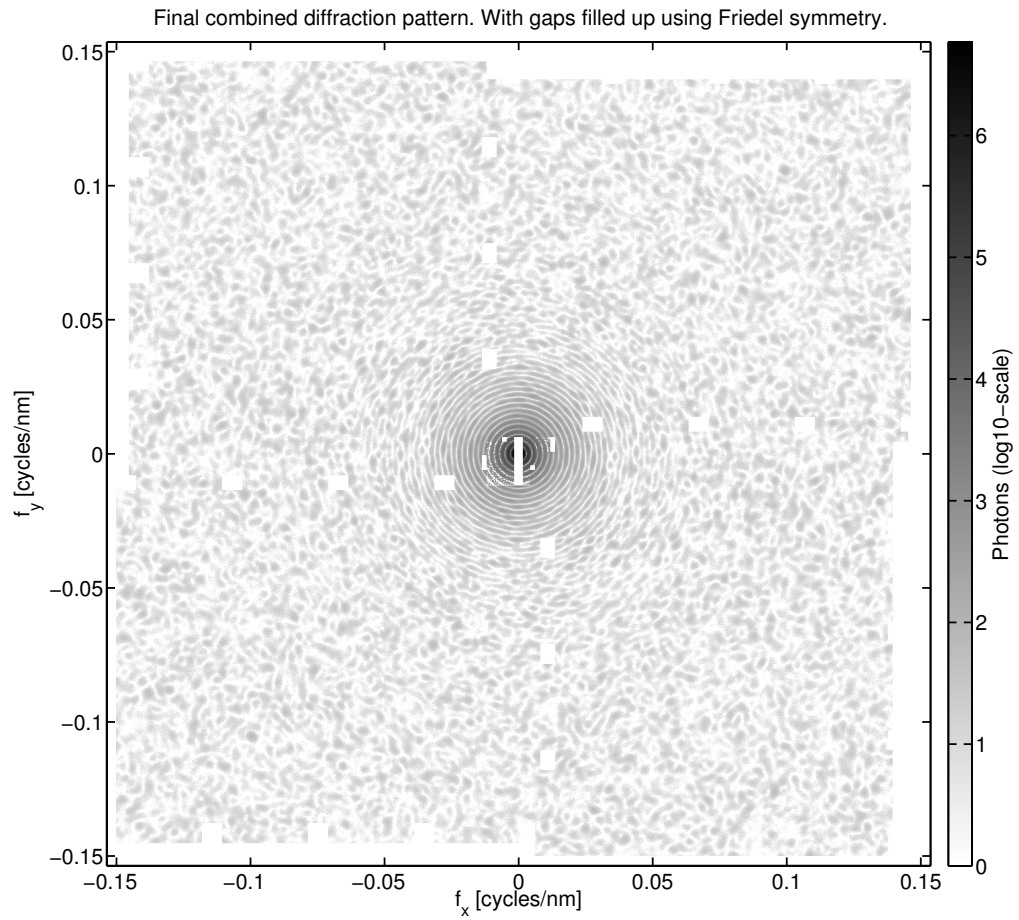


Figure 5.15: Simulated diffraction pattern obtained by filling up non-sensitive regions using Friedel symmetry. The original diffraction pattern from which this pattern was produced is shown in Figure 5.14.

5.3.4 1500 nm case

Lastly, the case of a very large particle with a diameter of 1500 nm is considered. The corresponding diffraction pattern, simulated for a sampling ratio of 5, is shown in Figure 5.16.

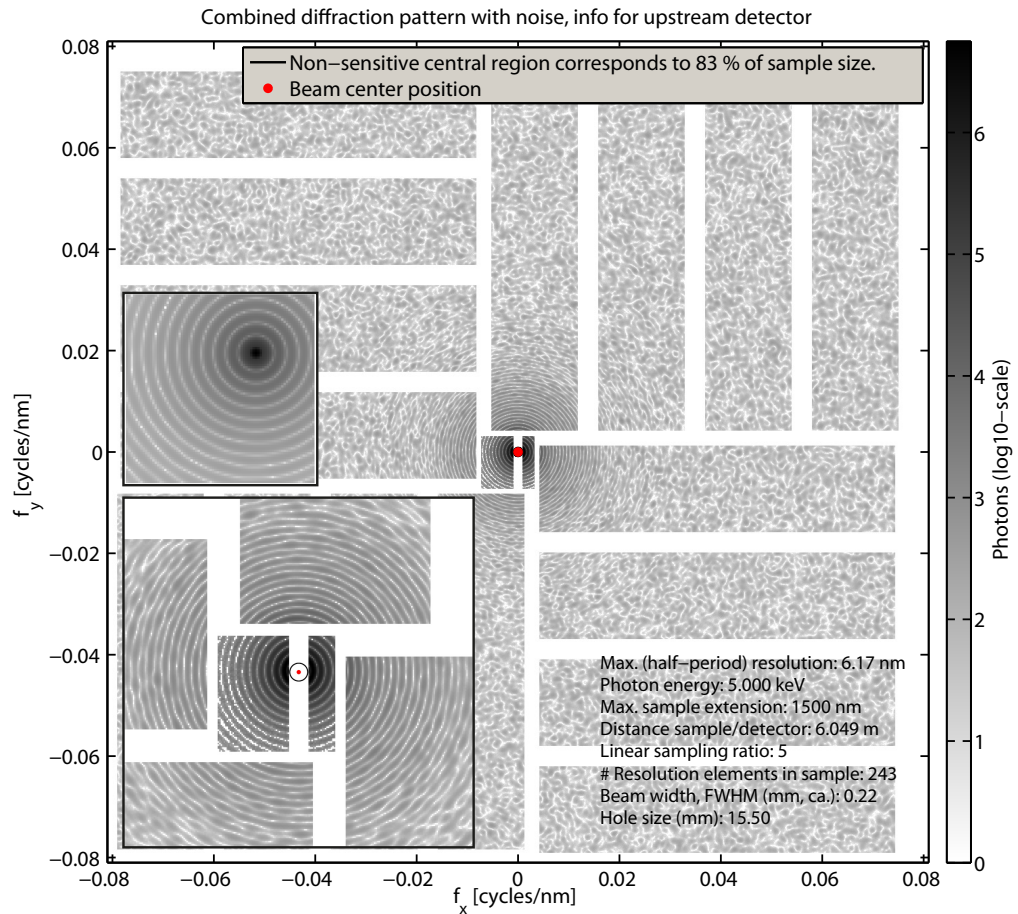


Figure 5.16: Simulated diffraction pattern for a 1500 nm particle at a sampling ratio of 5. Two detection planes are used to record the diffraction data. The large inset shows the central region of the combined diffraction pattern with noise. The small inset shows, for comparison, part of the diffraction pattern that corresponds to the area of the central hole in the upstream detector. It can be seen that the central speckle is essentially not measured.

5.4 Summary and conclusion

A summary of important geometrical parameters used for the simulations is shown in Figure 5.1. Note that all these simulations have been performed assuming a photon energy of 5 keV.

Table 5.1: Summary of important parameters used for the simulated study cases for the AGIPD detector.

	Small particles (20 nm)		Large particles (500 nm)			Huge particles (1500 nm)	
Detection planes	1	1	1	2	2	2	2
Module layout	Pile	Windmill	Pile	Pile	Windmill	Pile	Windmill
Upstream sample–detector distance [m]	0.403	0.403	1.613	3.226	3.226	5.47	6.17
Sampling ratio	25	25	4	8	8	5	5
Geometrical half-period resolution [nm]	0.39	0.40	1.57	2.97	3.25	5.47	6.17
Number of half-period resolution elements within sample	51	50	319	168	153	274	243
Width of upstream hole [mm]	2.2	2.2	2.2	9.8	12.80	15.1	15.50
Downstream sample–detector distance [m]	n.a.	n.a.	n.a.	6.452	6.452	9.026	10.181
Width of downstream gap [mm]	n.a.	n.a.	n.a.	2.0	2.0	1.5	1.5
Beam width in focus, intensity FWHM [μm]	0.1	0.1	1.0	1.0	1.0	3.0	3.0
Unique reconstruction possible? (as far as detector geometry is concerned)	Yes	Yes	No	Usually, yes	Usually, yes	Maybe in some cases	Maybe in some cases

Keeping these parameters in mind and considering the simulation results shown in the previous chapters, the following conclusions can be drawn:

■ Detection planes

For small reproducible objects from which many diffraction patterns are collected for a single dataset, one detection plane is sufficient. For large ($L \gtrsim 500$ nm) non-reproducible particles for which a reconstruction has to be obtained from a single diffraction pattern, two detection planes are required in order to obtain reconstructible datasets at resolutions that are possible given the expected number of scattered photons. Here, the upstream detector with an area of 16 modules covers most of the diffraction pattern, while the downstream detection

plane has to cover only a small area that can usually be covered by two modules.

- **Distance between detection components**

Depending on the size of the sample and the photon energy, the required sample-to-detector distance varies by a factor of about 1.5 to 2.5 between the upstream and downstream detector. As a consequence, a distance of several metres has to be foreseen between the two detection components. The required accuracy of the quadrant movement is on the order of 10% of the pixel pitch. Encoder control of the quadrant movement is thus essential to allow for a reliable mapping of the physical detector grid onto a numerical analysis grid.

- **Pile and windmill options**

Regarding possible detector layouts, two possible options have been identified for the large upstream detector: Either the so-called “pile” or the so-called “windmill” option. Based on the results obtained here, no clear preference can be given for one of these two options. However, the windmill option is a bit more advantageous, due to its slightly smaller dead area close to the centre as well as its more quadratic overall layout.

- **Gap option**

The so-called “gap” option has been ruled out here. It can, however, be advantageous in certain experimental situations to create this geometry. This is possible if either in the pile or in the windmill layout all four quadrants can be moved independently. Therefore, this option would be desirable, even though the main configuration is a centrosymmetric synchronized arrangement of all four quadrants as in an iris aperture (see Figures 5.5 and 5.12).

- **Decentering the upstream detector**

In order to decenter the upstream detector from a centrosymmetric position with respect to the beam, the whole detector needs to be movable in a plane perpendicular to the optical axis by a few centimeters. Such a translation could also be achieved by a synchronized translation of all four quadrants by the same vector.

- **Hole width**

It should be possible to vary the hole width between about 2 mm to at least 2.5 cm.

- **Downstream modules**

If possible, it would be advantageous to produce the downstream modules in such a way that, placed next to each other, they form a square active area instead of an elongated rectangle. In this way, one could cover the free area of a quadratic central hole better. On the other hand, this requirement can be mitigated if the central hole can be made rectangular instead of quadratic. This, however, again requires independently movable quadrants.

6 Considerations on the optimum DSSC module layout

The DSSC detector, under development by the DSSC detector consortium for the European XFEL, is optimized for low photon-beam energies, between 500 eV and 6 keV. The main design parameters and performance details of the detector can be found elsewhere [10]. Here, the parameters that are most relevant for the use of the detector at the SPB station will be discussed.

As the DSSC detector will combine single-photon sensitivity with a high dynamic range also at low photon-beam energy, it is particularly suited to cover the lower energy range of the SPB station (3–5 keV). The analysis presented above for the AGIPD detector was repeated for the DSSC taking into account:

- Different dynamic range of the DSSC with respect to the AGIPD and with respect to varying photon energies
- DSSC detector geometry, including gaps and inactive areas, and the fact that the pixels have a hexagonal shape

Although both cases—photon energies $E_\gamma = 5$ keV and 3 keV—have been investigated, in the remainder of the chapter, only the case of 3 keV will be considered, to show the complementarity with respect to the AGIPD detector.

6.1 Overview of the relevant DSSC parameters

6.1.1 Dynamic range

The values of the dynamic range of the DSSC detector have been taken from [10]. The achievable dynamic range of the DSSC, expressed in number of photons, depends on many factors, which are summarized in [10]. Here, it is worth mentioning that these factors include the photon energy and the number of bins of the Analog-to-Digital Converter (ADC). In the simulation presented here, an energy-dependent dynamic range was considered (the best achievable while maintaining single-photon sensitivity and considering a 9-bit ADC). For a 3 keV photon beam, this corresponds to a dynamic range of 23 220 photons.

6.1.2 Simulation strategy

The same strategy used for the AGIPD detector was used for the DSSC simulation. The details can be found in Section 5.0.2, “Simulation strategy”.

6.1.3 Considerations on the geometry and on the hexagonal pixel shape

The DSSC detector is a silicon pixel detector with 1024×1024 active pixels. A single detector module has 128×256 pixels and two detector modules build up a ladder, the basic detector structure, which is made of 128×512 pixels. Four ladders placed horizontally next to each other constitute a quadrant; the full detector is composed of four quadrants. The ladders and the quadrants are arranged such that the gap between them corresponds to an integer multiple of the pixel pitch in both the horizontal and vertical directions.

In particular:

- Vertical gap between the two sensors constituting a ladder corresponds to 8 pixels ($8 \times 236 \mu\text{m} = 1888 \mu\text{m}$).
- Vertical gap between the quadrants corresponds to 13 pixels ($13 \times 236 \mu\text{m} = 3068 \mu\text{m}$).
- Horizontal gap between the ladders and the quadrants corresponds to 20 pixels ($20 \times 204 \mu\text{m} = 4080 \mu\text{m}$).
- Minimal inactive area due to the presence of the central hole therefore has a size of $4080 \times 3068 \text{ mm}^2$.
- Central region of the detector has an inherent hole of $2.0 \times 2.5 \text{ mm}^2$. It corresponds to the aperture in the detector centre between the main support structures of the four quadrants.

In the baseline design (see the DSSC specification sheet), the detector is composed of 16 ladders, all having the same spatial orientation (the long side in the vertical direction). This allows the gaps between ladders and quadrants to be an integer multiple of the pixel pitch and allows all the hexagonal pixels to have the same orientation.

As mentioned above, the DSSC pixel has a hexagonal shape (see Figure 6.1) with a pixel pitch of 204 μm in the x (horizontal) and 236 μm in the y (vertical) direction, respectively. As a consequence, the centres of the pixels do not lie on a quadratic grid, as it is the case for the AGIPD. If n_x and n_y are the pixel numbers in a module, where $0 < n_x < 127$ and $0 < n_y < 255$, the coordinates of the pixel centres can be obtained from the following simple relations (see also Figure 6.1):

$$x_n = (0.5 + n_x)D, \quad (6.1)$$

$$y_n = (0.5 + n_y)D \sin(60^\circ) \quad \text{or} \quad (6.2)$$

$$= (1 + n_y)D \sin(60^\circ). \quad (6.3)$$

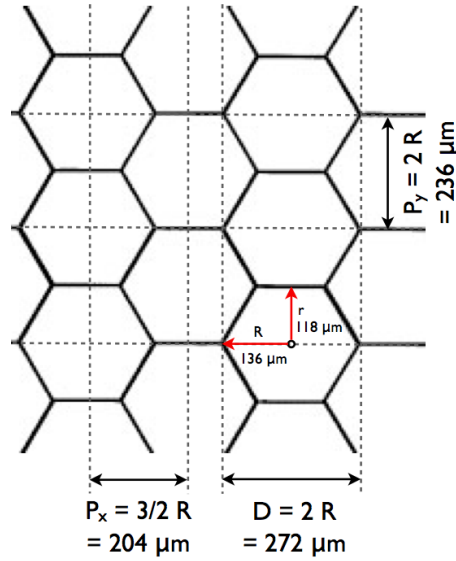


Figure 6.1: DSSC pixel dimensions

Here, $D = 2R$ is twice the side length of the hexagonal pixel. The formulae above indicate that the y position of the pixel centres is different for “even” and “odd” columns.

To correctly take into account the position of the pixel centres in the simulation of the diffraction pattern and of its mapping of the detector, a double grid structure was chosen. The number of “virtual” pixels in y was doubled, and the centre coordinates were chosen such that:

$$x'_n = (2.0 + n'_x)D/2, \quad (6.4)$$

$$y'_n = (1.0 + n'_y)D/2 \sin(60^\circ). \quad (6.5)$$

with $0 < n_x < 127$ and $0 < n_y < 511$. In this way, all the centre coordinates of the original pixels are represented by a point in a rectangular grid, at the price of adding the same amount of “virtual” centres. To correctly treat the effective number of pixels of the real detector, half of the “virtual” pixels are masked out when evaluating the map of the diffraction pattern on the detector. As a consequence, the detector module looks like a non-square chessboard, where the original hexagonal pixel has the same area as two rectangles in the chessboard, with the area of one rectangle being masked out (see Figure 6.2). The number of pixels in x and y is not the same anymore. This must be taken into account in determining the linear sampling ratio, the geometrical half-period resolution, etc. The fact that a real detector pixel is represented in the simulation by two rectangles, one white and one black, has also to be taken into account when the saturation threshold is determined to see if the signal on a given pixel causes its saturation. As the area of the white pixel is half that of a hexagonal pixel, the number of photons that saturate the white pixels is half of the number of photons that cause saturation of a hexagonal pixel. As a consequence, the saturation level for the white pixels was reduced in the simulation code to half the saturation level of the DSSC pixels.

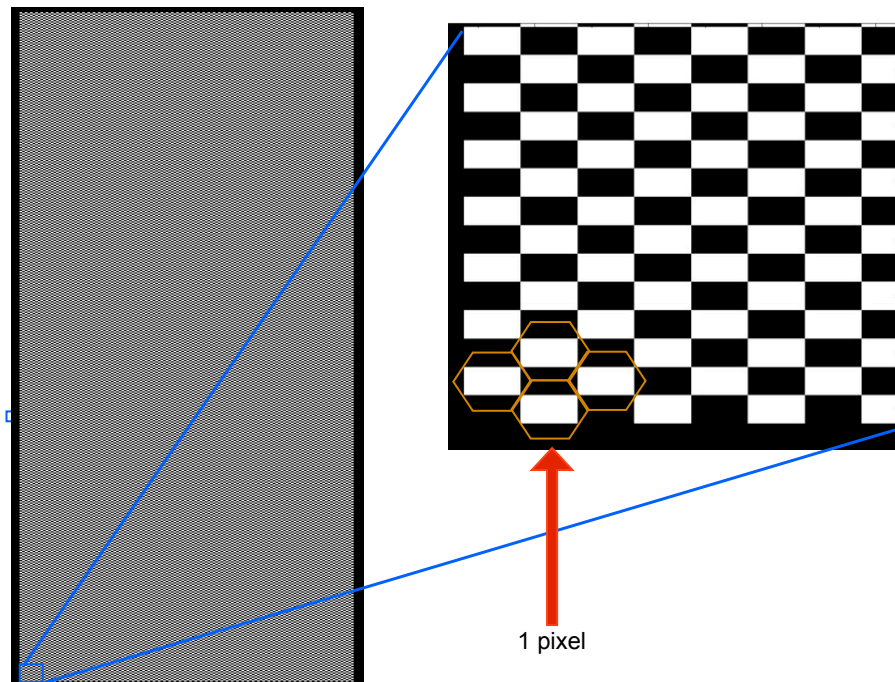


Figure 6.2: Chessboard treatment of the hexagonal pixels in the simulation

This solution represents a first-order approximation for the treatment of the hexagonal pixel. However, more sophisticated approaches, not needed for the study presented

here, are possible. Nevertheless, from a theoretical point of view, the model is exact if the measurement process is regarded as an ideal point-sampling process of a continuous 2D scalar field.¹

Note that the sampling period of the hexagonal grid differs in two ways from the sampling period of the quadratic Cartesian grid used for the AGIPD simulations: Firstly, only every second pixel of the rectangular grid that is used to describe the hexagonal grid carries information. As a consequence, the effective sampling period is lower than for the Cartesian grid used for the simulation. As the valid rectangular pixels, however, are arranged on two interlaced rectangular grids with a period corresponding to two rectangles in horizontal and vertical direction, the effective sampling period is not exactly half the sampling period of the simulation grid (see Figure 6.2). Secondly, due to the non-square pixel grid, sampling in the horizontal and vertical direction is not exactly the same, but, with a value of 1.16 : 1, the aspect ratio is close to 1, and the effects of this asymmetry were not studied here. All mentioned sampling ratios refer to the horizontal direction and the period of the simulation grid (i.e. half of the period corresponding to each individual interlaced grid).

As for the AGIPD, the baseline (pile) and windmill options were considered in the simulation for the DSSC detector. However, the gap option was not considered, as it was already clear from the AGIPD analysis that it presented disadvantages with respect to the others. In the DSSC case—with an existing baseline mechanics design for the pile option—the aim was to understand if adopting the windmill design could provide a largely improved detector performance. Both in the baseline and in the windmill option, a detector configuration in which the four quadrants can be moved independently—as foreseen in the present design—was considered.

¹This is sampled here on the centres of rectangular pixels that are arranged on a grid that can be mapped onto a hexagonal pixel grid whose grid points (the pixel centres) coincide with each second pixel centre in the Cartesian grid (see Figure 6.2).

6.2 Windmill option

For the DSSC detector, the windmill design implies that the ladder orientation is not always the same, as in the baseline design, but differs in the different quadrants (see Figure 5.11). All four quadrants are free to move independently. The investigated case was the scattering of 10^{12} 3 keV photons from a 20 nm particle (for the description of the sample features, see the AGIPD case). The beam focus had a size of 100 nm. The linear sampling ratio was chosen to be $\sigma = 25$ and the detector hole kept as small as possible. In these conditions, the distance between the sample and the detector is ~ 25 cm.

To evaluate the performance difference of the two designs, due to the choice of the windmill or baseline (pile) design, the simulation was performed using either the baseline or the windmill detector geometry. The results for the windmill and baseline design are shown in Fig. 6.3, top and bottom, respectively. The performance of the DSSC detector is very similar to that of the AGIPD. The geometrically limited resolution is 0.42 nm. No significant difference was observed between the two configurations in terms of performance and expected resolution. As the expected conclusion is the same for larger particles, and as a mechanics concept exists for the baseline design, the windmill option was no longer considered.

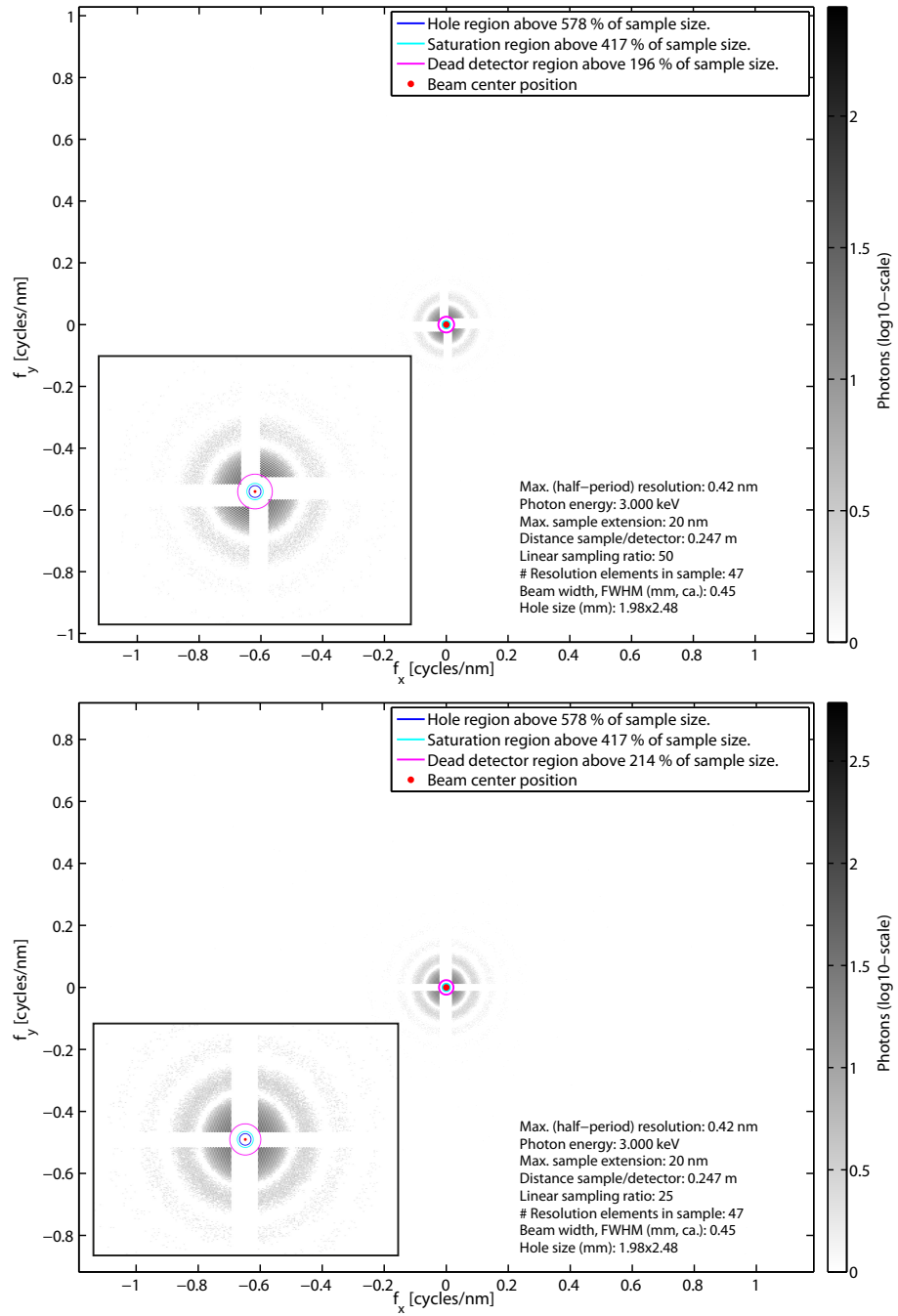


Figure 6.3: Diffraction pattern of a 20 nm particle on the DSSC detector, for the windmill (top) and baseline (bottom) design. In both charts, the insets represent a magnified view on the centre region.

6.3 Baseline (pile) option

In the baseline detector option, as mentioned above, all the ladders and therefore all the pixels have the same orientation (see Figure 5.4), the gaps between ladders and quadrants correspond to an integer multiple of the pixel pitch, and the four quadrants are all independently movable. The inactive area has a minimal size of 20 pixels in the horizontal direction and 13 pixels in the vertical direction. Keeping the hole and the inactive area size to a minimum, the simulation of a diffraction pattern was performed assuming 10^{12} 3 keV photons, with a focus size of $1\ \mu\text{m}$, incident on a sample with a diameter of 500 nm. The results are shown in Figure 6.4 and Figure 6.5.

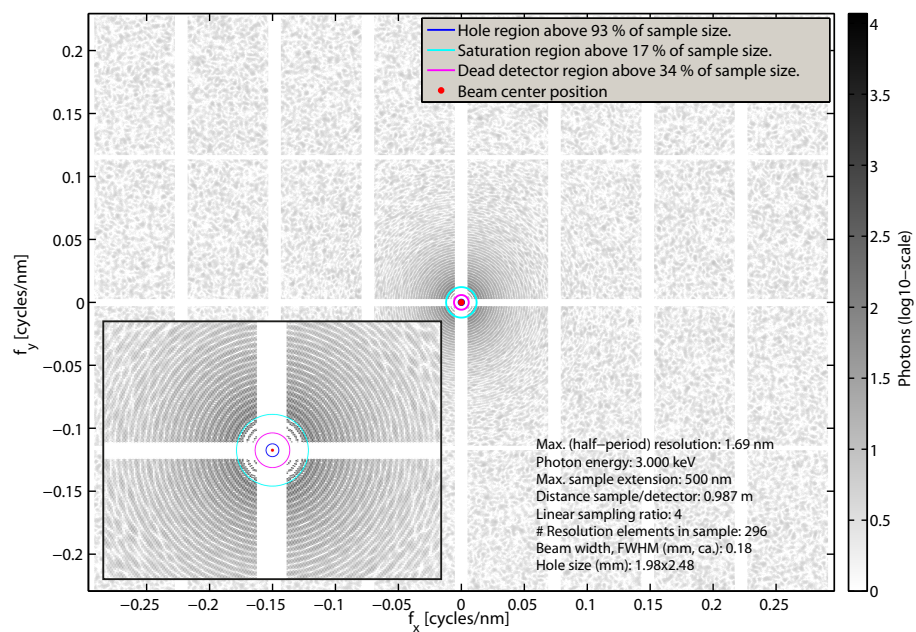


Figure 6.4: Diffraction pattern from a 500 nm particle on a single DSSC detector plane, with a linear sampling ratio of 4. The inset shows a magnified view on the central region. White areas within the sensitive detector regions correspond to saturated regions.

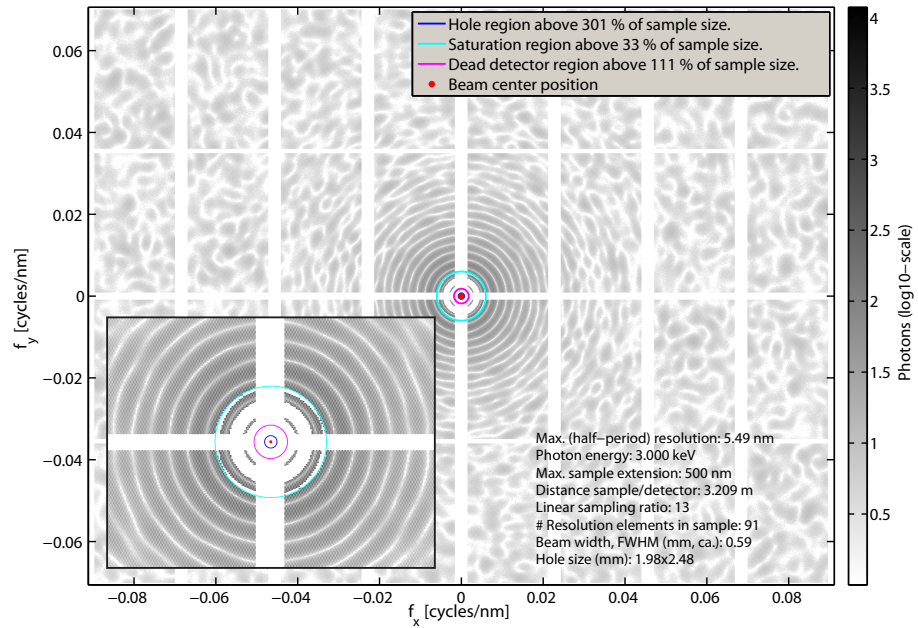


Figure 6.5: Diffraction pattern due to a 500 nm particle on a single DSSC detector plane, with a linear sampling ratio of 13. The inset shows a magnified view on the central region. White areas within the sensitive detector regions correspond to saturated regions.

When the linear sampling ratio is fixed to $\sigma = 4$, which allows the best practically achievable resolution, a lot of information about the low-frequency data are not recorded in the detector due to the central inactive area. For these large samples, this prevents a quantitative reconstruction from the diffraction pattern.

For $\sigma = 13$, which is the lowest accessible sampling ratio given the necessary width of the central inactive area, part of the low-frequency data still cannot be recorded because the innermost active area of the detector is saturated by the strong diffraction signal. Thus, in this case, the reconstruction of the sample is not possible either. An even larger σ would allow to distribute the signal over more pixels, but at the price of a poor resolution. The same is true for using an attenuator, which could allow measurements in the now-saturated regions close to the centre but would substantially suppress the high-q scattering signal.

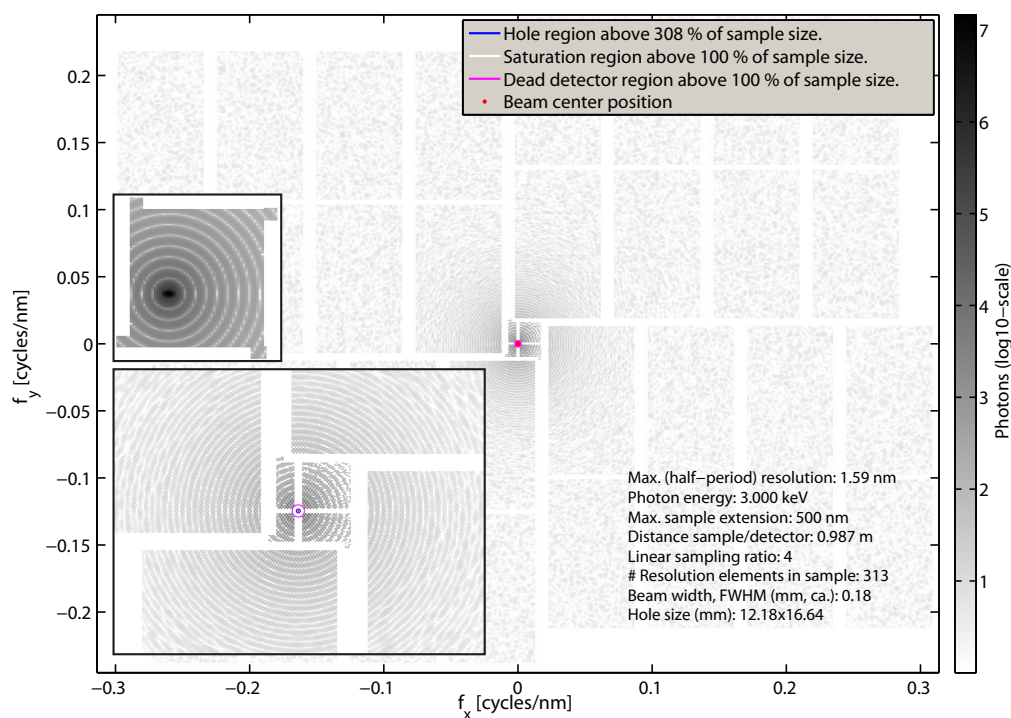


Figure 6.6: Diffraction pattern from a 500 nm particle on a DSSC detector composed of an upstream and a downstream plane, with a linear sampling ratio of 4. The lower left inset is a zoom into the innermost detector part showing the contribution of the second detector plane. In addition, the fraction of the diffraction pattern transmitted through the central hole of the upstream detector is shown. Note that the colour scale does not correspond to the small inset.

The conclusion for a 500 nm particle is therefore the same as obtained for the AGIPD detector: a single detector plane is not sufficient to record the low-frequency data, and this configuration therefore prevents a complete analysis for those particles. A possible way to recover low-frequency data is the use of a second detector plane, to be placed downstream of the first one. The aperture in the first detector plane has to be large enough to avoid saturation in the central detector regions, and an attenuator with a central hole for the direct beam has to be placed between the two detector planes in order to avoid saturation on the second plane. The solution tested for the DSSC is similar to that used for the AGIPD: a full DSSC detector is placed upstream and a two-ladder plane is put downstream. The distance between the first and the second detector plane is in principle a free parameter, as long as the solid angle opened up by the front detector central hole is covered by the back detector. In this case, it was chosen (whenever possible) to be twice the distance between the sample and the first plane.

A difference with respect to the AGIPD case is that the lower photon energy causes

the sample to diffract stronger, and therefore larger numbers of photons per pixel are expected in the central detector regions. Moreover, the DSSC saturation threshold at 3 keV is lower than that of the AGIPD (23 200 photons to be compared with 40 000 for the AGIPD, which does not achieve single-photon sensitivity at those energies). To be able to record the signal on the upstream detector plane without saturating it, an appropriately large aperture has to be chosen. This drives the choice of the area of the second detector plane, which has to record the signal passing through the aperture in the first plane. For the cases presented in the following, a four-module (two-ladder) detector system was chosen, with a minimal central hole size equal to that of the full-detector hole.

Another approach would be to attenuate the signal also in front of the first detector plane to keep the hole size small enough to be able to detect the transmitted signal with a two-module downstream detector. This approach was also investigated, but the results are not shown here. Although the best detector configuration in terms of aperture size of the first plane, area of the second plane, and so on are affected by this kind of choice, the overall conclusion of the study is not changed. Therefore, in the following, we will focus, whenever possible, on the results obtained by attenuating the signal only in front of the second detector plane.

The results for 10^{12} 3 keV photons, with a focal size of 1 μm , impinging on a 500 nm sample, are shown in Figure 6.6 and Figure 6.7. The two cases, $\sigma = 4$ and $\sigma = 8$, have been considered. In the case of $\sigma = 4$, the second detector plane had to be placed at a distance from the sample equal to four (and not two) times the distance between the sample and the first detector plane. This is possible as the distance between the sample and the first detector plane is, in this case, a bit less than 1 metre (see Figure 6.6). For the case of $\sigma = 8$, the distance between the sample and the second detector plane was twice the distance between the sample and the first plane. In the bottom part of the figures, for each of the two cases, a zoom to the innermost detector part is shown. The second detector plane and the part of the signal recorded there can be clearly recognized.

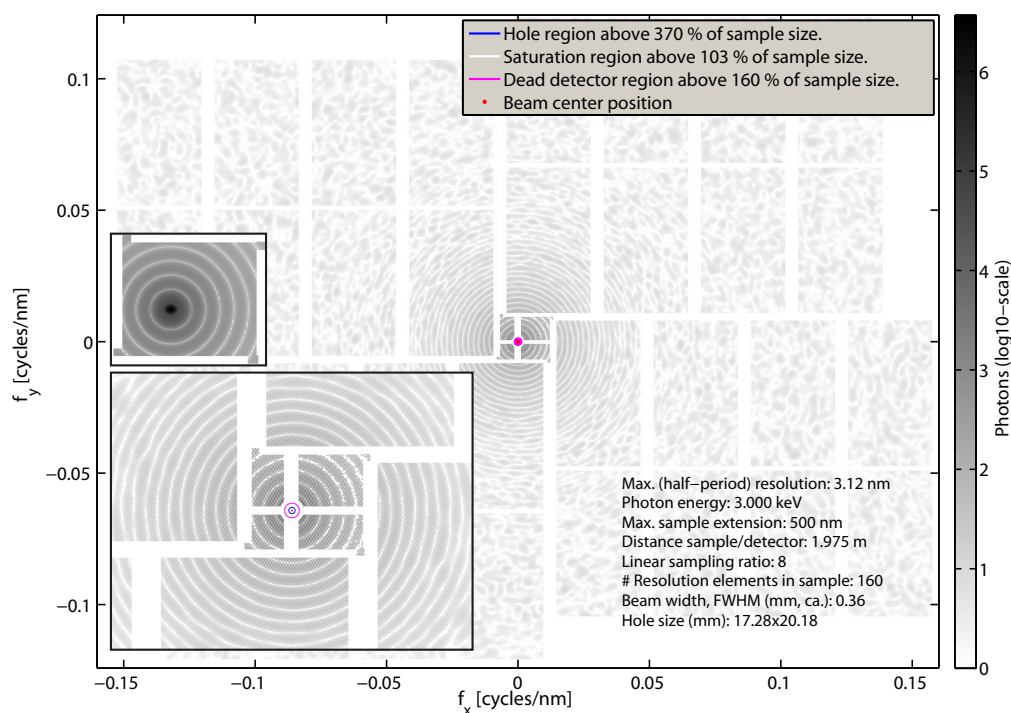


Figure 6.7: Diffraction pattern from a 500 nm particle on a DSSC detector composed of an upstream and a downstream plane, with a linear sampling ratio of 8. The lower left inset is a zoom into the innermost detector part, showing the contribution of the second detector plane. In addition, the fraction of the diffraction pattern transmitted through the central hole of the upstream detector is shown. Note that the colour scale does not apply to the small inset.

In this case, the signal on the second plane requires an attenuation of a factor 80 in order to prevent saturation. The combination of the images from the first and the second detector plane allows the recovery of the low-frequency data and enables therefore, in principle, a quantitative reconstruction, both with low ($\sigma = 8$, resolution 3.1 nm) and high ($\sigma = 4$, resolution 1.6 nm) resolutions. Due to the complicated mask structure describing the hexagonal-pixel grid, the use of Friedel symmetry is not as simple in this case as it is for the quadratic AGIPD pixel grid (see the previous chapter).

Another case considered is that of an even larger particle, 1.5 μm in diameter, illuminated by 10^{12} 3 keV photons in a beam with a focus size of 3 μm . In this case, the need for the second detection plane is even higher as the fringe period decreases and the dynamic range of the diffracted signal increases. In this case, a signal attenuation also in front of the first detector plane was necessary. The sample-detector distance in this case is almost four meters, so that the second detector plane has to be situated at a large distance from the sample. Simulation

results are shown in Figure 6.8 for the $\sigma = 5$ case. The signal in front of the first detector plane is attenuated by a factor of 5, in front of the second detector plane by another factor of 67, applied to the already attenuated signal that has passed the upstream detection plane. With this configuration, the low-frequency data can be recovered.

Note that, in both cases, the attenuators require a central hole so that the non-scattered beam does not interact with the attenuator material. Furthermore, the effects of parasitic scattering signal originating from the edges of the attenuators have to be suppressed as much as possible. One possibility here is to minimize the distance along the optical axis between the attenuator and the corresponding detector.

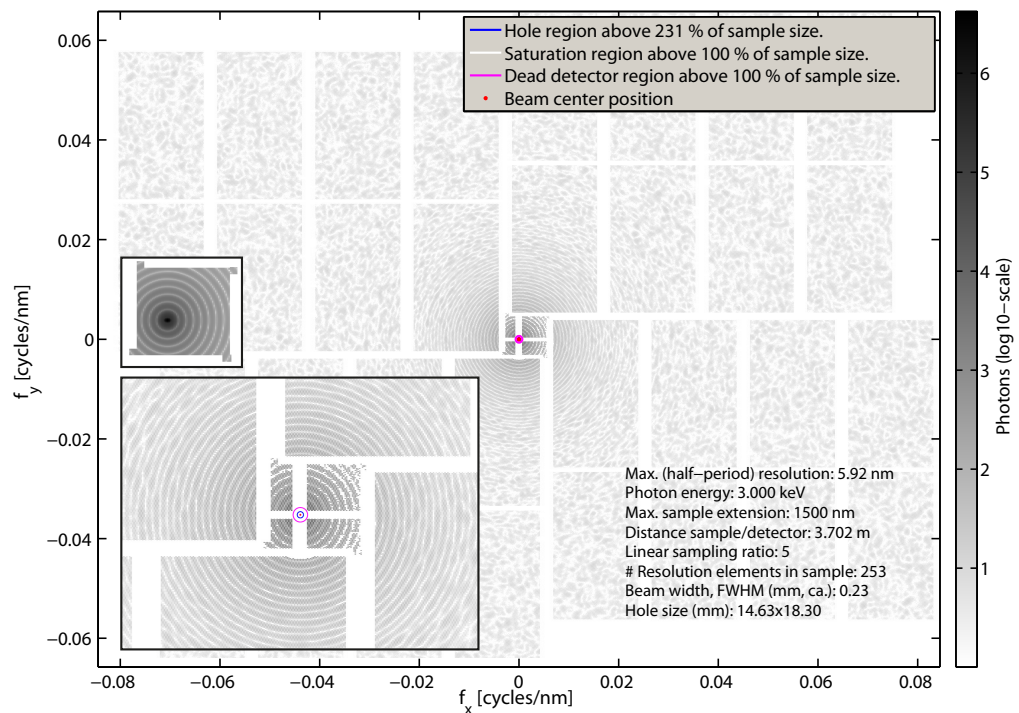


Figure 6.8: Diffraction pattern from a $1.5 \mu\text{m}$ particle on a DSSC detector composed of an upstream and a downstream plane, with a linear sampling ratio of 5. The large inset represents a magnified view on the central detector region, whereas the small inset illustrates the diffraction passing the central hole of the upstream detector. Note that the colour scale does not apply to the small inset.

6.4 Summary and conclusion

A summary of important geometrical parameters used for the simulations is shown in Figure 6.1.

Table 6.1: Summary of important parameters used for the simulated study cases for the DSSC detector. Note that for these simulations the photon energy has been set to a value of 3 keV.

	Small particles (20 nm)		Large particles (500 nm)			Huge particles (1500 nm)	
Detection planes	1	1	1	1	2	2	2
Module layout	Baseline (pile)	Windmill	Baseline (pile)	Baseline (pile)	Baseline (pile)	Baseline (pile)	Baseline (pile)
Upstream sample-detector distance [m]	0.247	0.247	0.987	3.209	0.987	1.975	2.962
Sampling ratio	25	25	4	13	4	8	4
Geometrical half-period resolution [nm]	0.42	0.42	1.69	5.49	1.62	3.23	4.84
Number of half-period resolution elements within sample	47	47	296	91	308	154	309
Width of upstream hole [mm]	2.0 x 2.5	2.0 x 2.5	2.0 x 2.5	2 x 2.5	8.1 x 10.0	9.12 x 10.74	9.1 x 10.7
Downstream sample-detector distance [m]	n.a.	n.a.	n.a.	n.a.	1.974	3.950	5.924
Width of downstream gap [mm]	n.a.	n.a.	n.a.	n.a.	2.1	2.1	2.1
Beam width in focus, intensity FWHM [μm]	0.1	0.1	1.0	1.0	1.0	1.0	3.0
Unique reconstruction possible? (as far as detector geometry is concerned)	Yes	Yes	No	Usually, yes	Usually, yes	Maybe in some cases	Maybe in some cases

Building on the simulation results, these parameters, and the results obtained for the AGIPD case, it becomes clear that very similar conclusions can be drawn for the case of the DSSC detector.

We thus do not reiterate those conclusions here (see Section 5.4, “Summary and conclusion”). The only and minor difference refers to the comparison of the baseline (pile) case and the windmill design. For the DSSC detector, the difference is even less evident than for the AGIPD detector, and thus, as the pile design is currently in progress, the windmill design has been not considered any further.

In addition, one may combine a downstream AGIPD detector with an upstream DSSC detector in order to simplify operation. Even though the AGIPD detector is

not primarily designed for lower photon energies around 3 keV, the downstream AGIPD module will probably be sufficient, as the low-q diffraction that reaches the downstream detector usually implies a high photon count per pixel and thus does not require single-photon sensitivity. Such a hybrid solution would, however, imply the necessity to bring the different sampling grids of both detectors into one numerical grid. This is expected to be feasible, as the interpolation of the downstream grid onto the upstream grid works well for the expected high photon count rates for the downstream plane.

7 Overall conclusions

The purpose of this document is to investigate the feasibility of different detector layouts and geometries with respect to applications in coherent imaging at the SPB instrument of the European XFEL. Two detector designs, currently developed and implemented by the AGIPD and the DSSC consortia, are considered, with an emphasis on an accurate mathematical representation of the geometrical parameters, as far as they influence the experimental feasibility.

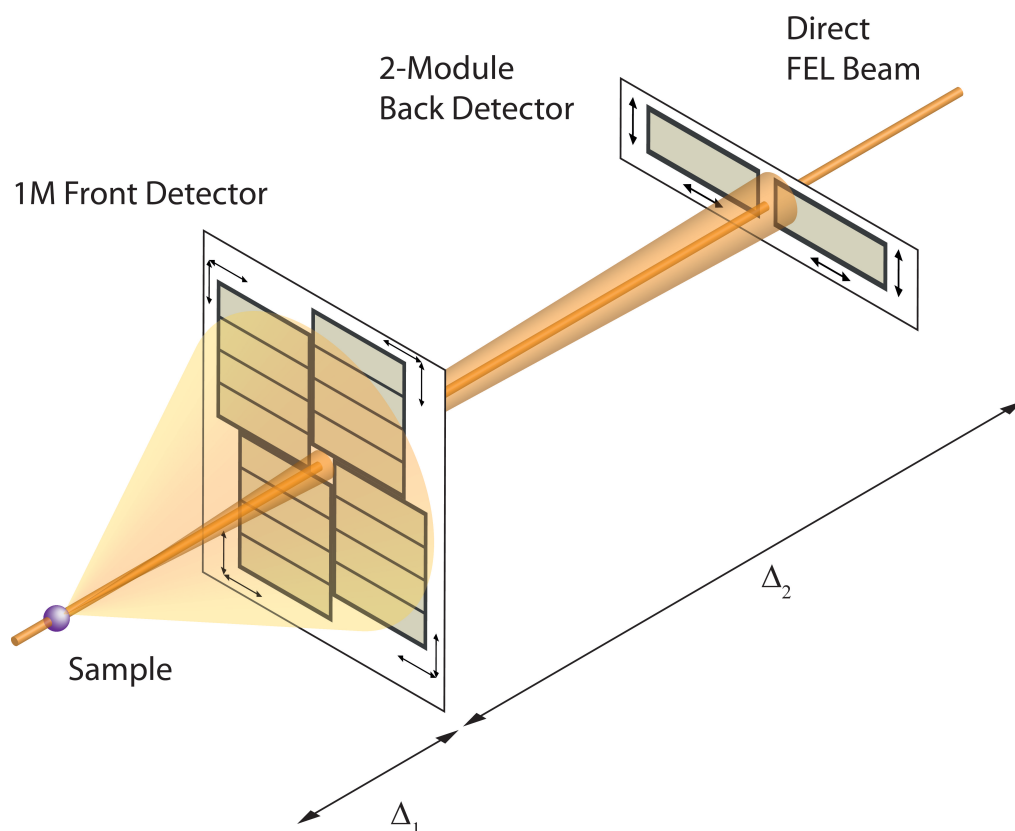


Figure 7.1: Possible layout for coherent single-particle imaging at the SPB instrument: The front detector collects the high-angle, high-resolution scattering contributions, whereas the rear detector collects the small-angle, low resolution information. Depending on the size of the sample, the wavelength of the radiation, and the desired resolution, the sample-detector distance Δ_1 —for non-crystallographic samples—varies between less than 25 cm and approx. 5 m, while the sample-detector distance $\Delta_1 + \Delta_2$ of the rear detector varies between about 5 m and 10 m.

Even though the two detectors are relatively different in design and only partially overlap in their applicable photon energy ranges, the general conclusions drawn here are very similar.

A possible detector layout for single-particle imaging that is in agreement with the conclusions of this document is shown in Figure 7.1. Here, a typical two-plane-detection setup is shown with a large front and a small back detector. The layout of the two detector panels corresponds to a possible AGIPD layout as explained before (16 quadrants in pile configuration, see Section 5.2, “Pile option”, for the upstream detector, two quadrants aligned with their long side in horizontal direction for the downstream detector).

Those conclusions are:

- **Detection planes**

Imaging of small particles, i.e. macromolecules or atomic clusters, is geometrically feasible with a single detection plane for both the AGIPD and the DSSC detector. For larger particles, however, such as viruses or organelles, a transition to two detection planes is inevitable in order to fully cover the Fourier space that can be accessed in a single pulse with the expected photon densities.

- **Two-plane detection setup**

A feasible two-plane detection setup for both detector concepts consists of a large 1 M upstream detector (high resolution, high q -values) and a small downstream detector (low resolution, low q -values) at a distance 1.5 to about 4 times away from the sample compared to the upstream detector.

- **Upstream detector**

The upstream detector is ideally composed of 4 quadrants that can be translated individually in the plane of detection. This allows for (i) the necessary adjustment of the central hole diameter to small or large particle experiments and (ii) the adaption of the quadrant layout to the expected scattering signal. As an example, the strong linear stripe caused by diffraction from the edges of a liquid jet used for sample injection could be directed into a linear gap between individually movable quadrants.

- **Detector layouts**

Three different detector layouts for the upstream detector have been investigated, most importantly the so-called “pile” or “baseline” option (see Figure 5.4) and the so-called “windmill” option (see Figure 5.11). With respect to the envisioned experiments, they differ only in minor details, so that, for the DSSC detector, the baseline design can safely be regarded as a viable option. For the AGIPD detector, a decision should incorporate the ease of implementation and maintenance for both options.

- **Downstream detector**

The downstream detector can consist of a much smaller active area, as it is required to cover a much smaller area in q -space. In the case of the AGIPD detector, a combination of two modules could be used that are facing each other along their short sides and that have a narrower non-sensitive ring than the longer sides.

- **Central hole**

To accommodate single-plane coherent imaging for small particles, such as molecules, and two-plane imaging of larger particles, the central hole is required to be variable between about 2 mm and 25 mm.

For further details, see Section 5.4 and Section 6.4.

8 Bibliography

- [1] H. N. Chapman et al. “Femtosecond X-ray protein nanocrystallography”. In: *Nature* 470.7332 (Feb. 2011), pp. 73–77. DOI: [10.1038/nature09750](https://doi.org/10.1038/nature09750).
- [2] H. N. Chapman et al. “High-resolution ab initio three-dimensional x-ray diffraction microscopy”. In: *Journal of the Optical Society of America A* 23.5 (2006), p. 1179. DOI: [10.1364/JOSAA.23.001179](https://doi.org/10.1364/JOSAA.23.001179).
- [3] K. Giewekemeyer. *A study on new approaches in coherent x-ray microscopy of biological specimens*. Göttingen series in x-ray physics , ISSN 2191-9860. Göttingen: Univ.-Verl. Göttingen, 2011.
- [4] B. Henrich et al. “The adaptive gain integrating pixel detector AGIPD a detector for the European XFEL”. In: *Nuclear Instruments and Methods in Physics Research Section A: Accelerators, Spectrometers, Detectors and Associated Equipment* 633, Supplement 1.0 (May 2011), S11–S14. DOI: [10.1016/j.nima.2010.06.107](https://doi.org/10.1016/j.nima.2010.06.107).
- [5] X. Huang et al. “Incorrect support and missing center tolerances of phasing algorithms”. In: *Optics Express* 18.25 (Dec. 2010), pp. 26441–26449. DOI: [10.1364/OE.18.026441](https://doi.org/10.1364/OE.18.026441).
- [6] X. Huang et al. “Signal-to-noise and radiation exposure considerations in conventional and diffraction x-ray microscopy”. In: *Optics Express* 17.16 (July 2009), p. 13541. DOI: [10.1364/OE.17.013541](https://doi.org/10.1364/OE.17.013541).
- [7] N.-T. D. Loh and V. Elser. “Reconstruction algorithm for single-particle diffraction imaging experiments”. In: *Physical Review E* 80.2 (2009), p. 026705. DOI: [10.1103/PhysRevE.80.026705](https://doi.org/10.1103/PhysRevE.80.026705).
- [8] A. P. Mancuso. *Conceptual Design Report: Single Particles, Clusters and Biomolecules (SPB)*. 2011. DOI: [10.3204/XFEL.EU/TR-2011-007](https://doi.org/10.3204/XFEL.EU/TR-2011-007).
- [9] K. A. Nugent. “Coherent methods in the X-ray sciences”. In: *Advances in Physics* 59.1 (2010), pp. 1–99. DOI: [10.1080/00018730903270926](https://doi.org/10.1080/00018730903270926).
- [10] M. Porro et al. “Development of the DEPFET Sensor With Signal Compression: A Large Format X-Ray Imager With Mega-Frame Readout Capability for the European XFEL”. In: *IEEE Transactions on Nuclear Science* PP.99 (2012), p. 1. DOI: [10.1109/TNS.2012.2217755](https://doi.org/10.1109/TNS.2012.2217755).
- [11] G Potdevin, U Trunk, and H Graafsma. “HORUS, an HPAD X-ray detector simulation program”. In: *Journal of Instrumentation* 4.09 (Sept. 2009), P09010–P09010. DOI: [10.1088/1748-0221/4/09/P09010](https://doi.org/10.1088/1748-0221/4/09/P09010).

- [12] H. Quiney. “Coherent diffractive imaging using short wavelength light sources”. In: *Journal of Modern Optics* 57.13 (2010), pp. 1109–1149. DOI: [10.1080/09500340.2010.495459](https://doi.org/10.1080/09500340.2010.495459).
- [13] M. M. Seibert et al. “Single mimivirus particles intercepted and imaged with an X-ray laser”. In: *Nature* 470.7332 (Feb. 2011), pp. 78–81. DOI: [10.1038/nature09748](https://doi.org/10.1038/nature09748).
- [14] The AGIPD consortium. *Adaptive Gain Integrating Pixel Detector (AGIPD) - System Parameters*. July 2012.
- [15] P. Thibault and V. Elser. “X-Ray Diffraction Microscopy”. In: *Annual Review of Condensed Matter Physics* 1.1 (2010), pp. 237–255. DOI: [10.1146/annurev-conmatphys-070909-104034](https://doi.org/10.1146/annurev-conmatphys-070909-104034).
- [16] P. Thibault et al. “Reconstruction of a yeast cell from X-ray diffraction data”. en. In: *Acta Crystallographica Section A* 62.4 (July 2006), pp. 248–261. DOI: [10.1107/S0108767306016515](https://doi.org/10.1107/S0108767306016515).
- [17] F. v. d. Veen and F. Pfeiffer. “Coherent x-ray scattering”. In: *Journal of Physics: Condensed Matter* 16.28 (July 2004), pp. 5003–5030. DOI: [10.1088/0953-8984/16/28/020](https://doi.org/10.1088/0953-8984/16/28/020).